Physics of Fluids

RESEARCH ARTICLE | JANUARY 02 2025

Crosswind-induced aero-performance deterioration of a vehicle passing by a hill with different windproof measures ✓

Hong He (何洪) ; Guo-Zhi Li (李国志) ; Wei-Chao Yang (杨伟超); Yi-Kang Liu (刘义康) ;
E Deng (邓锷) ✉

Physics of Fluids 37, 015116 (2025)
https://doi.org/10.1063/5.0244864

Articles You May Be Interested In

Wake dynamic characteristics of windproof structures in embankment–bridge sections along a high-speed railway under natural strong crosswinds

Physics of Fluids (May 2023)

Acceleration and Reynolds effects of crosswind flow fields in gorge terrains

Physics of Fluids (August 2023)

Effects of windbreak types on aerodynamics of high-speed trains traversing from flat ground to semi-cutting and semi-embankment under crosswinds

Physics of Fluids (July 2024)

AIP Publishing

Physics of Fluids ARTICLE pubs.aip.org/aip/pof

Crosswind-induced aero-performance deterioration of a vehicle passing by a hill with different windproof measures

Cite as: Phys. Fluids **37**, 015116 (2025); doi: 10.1063/5.0244864
Submitted: 22 October 2024 · Accepted: 4 December 2024 ·
Published Online: 2 January 2025

Hong He (何洪),[1] Guo-Zhi Li (李国志),[1,2] Wei-Chao Yang (杨伟超),[1,3] Yi-Kang Liu (刘义康),[1,2]
and E Deng (邓锷)[2,4,5,a)]

AFFILIATIONS

[1]School of Civil Engineering, Central South University, Changsha, People's Republic of China
[2]The Hong Kong Polytechnic University Shenzhen Research Institute, Shenzhen, People's Republic of China
[3]National Engineering Research Center of High-speed Railway Construction Technology, Changsha, People's Republic of China
[4]Department of Civil and Environmental Engineering, The Hong Kong Polytechnic University, Hung Hom, Kowloon, Hong Kong
[5]National Rail Transit Electrification and Automation Engineering Technology Research Center (Hong Kong Branch), Hung Hom, Kowloon, Hong Kong

[a)]**Author to whom correspondence should be addressed:** early.deng@polyu.edu.hk

ABSTRACT

In crosswind conditions, the vehicle's aerodynamic performance significantly deteriorates when passing by a hill, impacting driving stability. Roadside windproof measures are effective in mitigating this performance deterioration. This study aims to explore the changes in aerodynamic performance of vehicles as they pass by a hill under three distinct scenarios: without wind barrier, solid wind barrier, and ventilation wind barrier. A three-dimensional computational fluid dynamics (CFD) model of the hill–embankment–wind barrier–vehicle–air, integrating the improved delayed detached eddy simulation (IDDES) turbulence model and a porous medium model, is established. The correctness of the numerical simulation is verified through field tests and wind tunnel experiments. The main conclusions are as follows: (1) When the vehicle passes by a hill under the crosswind, its aerodynamic loads undergo complex and significantly increased variations. ΔC_x, ΔC_y, ΔC_z, ΔC_{mx}, ΔC_{my}, and ΔC_{mz} in the hill section without wind barrier are 2.79, 4.42, 5.18, 3.73, 4.45, and 2.73 times higher than those in the flat section. (2) The fluctuation amplitude of the aerodynamic loads and the maximum value of power spectral density (PSD) are the greatest under the solid wind barrier. Under the solid wind barrier, ΔC_x, ΔC_y, ΔC_z, ΔC_{mx}, ΔC_{my}, and ΔC_{mz} are 3.63, 2.16, 4.34, 2.93, 2.00, and 3.21 times that with ventilation wind barrier. (3) Crosswinds cause flow separation on the leeward side and alter wind speed due to the hill's shelter without wind barrier. Ventilated barriers lessen these effects, while solid wind barrier reverses the crosswind direction, increases turbulence, and results in more erratic wind patterns and pressure changes on the vehicle's surface. (4) Without wind barrier, more vortex structures form on the leeward side and rear of the vehicle, which are smaller and less numerous with ventilation wind barrier. Solid wind barrier causes continuous changes in vortex structure position and size, resulting in the most significant aerodynamic load variations. This study provides valuable insights for selecting wind protection measures in hill sections of expressways.

NOMENCLATURE

a_{ij}, b_{ij}	fitting parameters
C	the coefficient affected by Reynolds number (Re) and α
C_1, C_2	the viscous and resistance coefficient in the incoming flow direction
C_x, C_y, C_z, C_{mx}, C_{my}, C_{mz}	drag, lift, lateral force, rolling moment, yaw moment, nodding moment coefficient of the vehicle
ΔC_x, ΔC_y, ΔC_z, ΔC_{mx}, ΔC_{my}, ΔC_{mz}	amplitude of variation for the aerodynamic load coefficients
d_w	the distance from the wall
F_x, F_y, F_z, M_x, M_y, M_z	drag, lift, lateral force, rolling moment, yaw moment, nodding moment of the vehicle (kN, kN·m)
f_e	f_{hyb} the lifting function and mixing function
f_{dt}	the delay function of DDES

f_{step}	a function that provides a fast switching from RANS to LES at the depth of the boundary layer
κ	the Von Karmen constant
L, W, H	length, width, height of the vehicle (m)
$\mathbf{S}$	Ω the strain rate and rotation rate tensor normalized by the turbulence time scale
S_i	additional source terms
S_c and H_c	the side area and height of the vehicle (m^2, m)
S_t	S_o the total area of the porous media plate and open area of the porous media plate (m^2)
t	time (s)
t_p	D_p the thickness and diameter of the ventilation plate (m)
U_z, U	Z-direction speed, wind speed (m/s)
V	the vehicle speed (m/s)
ν_t	the vortex viscosity
$\lvert v \rvert$	ρ the velocity and density of air (m/s, kg/m^3)
ω	the specific dissipation rate
μ	the dynamic viscosity of air
α	permeability coefficient
$\sigma C_x, \sigma C_y, \sigma C_z, \sigma C_{mx}, \sigma C_{my}, \sigma C_{mz}$	standard deviation for the aerodynamic load coefficients

Abbreviation

CFD	Computational fluid dynamics
CFL	Courant number
FFT	Fast Fourier transform
FVM	Finite volume method
IDDES	Improved delayed detached eddy simulation
LES	Large eddy simulation
PSD	Power spectral density
RANS	Reynolds-averaged Navier–Stokes
Re	Reynolds number
UDF	User-defined function

I. INTRODUCTION

As highway construction in mountainous areas accelerates, it has become a common operational scenario for vehicles to pass by hills while driving on highways. However, when a vehicle passes by a hill at high speeds during periods of strong crosswinds, it is subjected to considerable thrust. This can compromise the driver's control, posing a significant risk to the safety of both the driver and passengers.[1–6] Traffic accidents triggered by powerful crosswinds are not uncommon.[7–10] Data released by China's National Bureau of Statistics indicate that adverse weather is responsible for approximately 20% of all road traffic accidents, with accidents induced by crosswinds constituting a significant 30% of that total. Figure 1 illustrates photographs of traffic accidents that have been caused by such crosswinds. Wind barriers, an effective infrastructure for mitigating the degradation of vehicle aerodynamic performance, are frequently deployed along highways. These barriers typically come in two varieties: solid and ventilated.

The rapid driving of a vehicle in a crosswind environment can lead to deteriorated aerodynamic performance, potentially causing the vehicle to side slip or overturn.[11–13] Ljungskog *et al.*[14] scrutinized the impact of wind tunnel geometry and boundary conditions on vehicle aerodynamic performance using a combination of numerical simulations and wind tunnel tests. Their analysis yielded precise predictions of the vehicles' drag coefficients. Sekulic *et al.*[15] conducted a comparative analysis of the lateral stability and path tracking capabilities of tractor-semitrailer and sport utility vehicle under one-year storm conditions. The findings indicate that, at the highest driving speed, sport utility vehicle exhibits lateral movement and lane deviation. Zhang *et al.*[16] analyzed the peak and average aerodynamic loads of three kinds of vehicles (passenger cars, tractors, and trucks) on the bridge through wind tunnel tests. The impacts of vehicle position, wind direction, and geometric shape on aerodynamic loads were studied.

Many scholars have paid attention to the varying aerodynamic performance of vehicles under different operating scenarios. For instance, some studies have explored the impact of bridge towers on the aerodynamic performance of cars, indicating that in strong crosswinds, the wind environment above the deck near the bridge tower of long-span cable-supported bridges changes significantly, which can easily lead to lateral instability accidents for vehicles.[17] Wang *et al.*[18] investigated the dynamic response and aerodynamic performance of vehicles traversing a tower bridge in crosswind scenarios employing overlapping grid technology. Huang *et al.*[19,20] employed the DES turbulence model to investigate the characteristics of the flow field structure around the vehicle when the vehicle traversing the tower bridge at high speed under crosswind conditions in various lanes and lanes with different adhesion coefficients. Yu *et al.*[21] analyzed the passage of typical two-axle vehicles through the tower bridge. They formulated a comprehensive driver–vehicle–crosswind (DVC) model, assessed the driving risk associated with vehicles navigating the tower bridge in crosswind conditions. Chen *et al.*[22] investigated the impact of windbreak hills on the aerodynamic traits of high-speed trains in crosswind conditions and elucidated the mechanism behind the degradation of the aerodynamic performance of trains. Furthermore, other researchers have investigated the deterioration of aerodynamic performance of cars during overtaking maneuvers.[23] Hammad *et al.*[24] employed numerical simulations to scrutinize alterations in aerodynamic characteristics when two vehicles drive in opposite directions under crosswind conditions, finding a 43% increase in aerodynamic load when vehicles intersect.

The placement of wind barriers along the roadside has proven to be a practical measure in mitigating the decline in aerodynamic performance induced by crosswind conditions, improve the safety and comfort of vehicle driving, and reduce the probability of traffic accidents.[25–27] Chen *et al.*[28] established a numerical model for a wind–vehicle–bridge coupling vibration system. They investigated how wind barriers affect driving safety in crosswind conditions, revealing that the presence of a wind barrier significantly enhances vehicle safety. The research on wind barrier mainly focuses on the type, height, and ventilation rate of wind barrier. Wang *et al.*[29] utilized the computational fluid dynamics (CFD) method to simulate the flow field around the vehicle and in the proximity of the wind barrier during both sound barrier-equipped and sound barrier-free driving scenarios. The investigation included an analysis of the impact of vehicle shape, sound barrier height, sound barrier shape condition, and the distance between the vehicle and the sound barrier on the aerodynamic loads experienced by the vehicle. Xue *et al.*[30] performed a series of wind tunnel tests to examine how wind barrier height and ventilation rate impact the aerodynamic characteristics of the wind–vehicle–bridge system.

FIG. 1. Traffic accidents caused by crosswinds: (a) rollover, Hang-Rui Expressway, Yunnan, China, 2022; (b) rollover, Hu-Ning Expressway, Jiangsu, China, 2022; (c) rollover, Yong-Jin Expressway, Zhejiang, China, 2020; and (d) lane departure, Tokyo, Japan, 2021.

The findings indicate that decreasing the ventilation rate and increasing the height of the wind barrier contribute to a reduction in lateral vehicle displacement. Xiang *et al.*[31] assessed the driving safety of vehicles in various wind barrier conditions. The findings reveal that the height of the wind barrier alters the effect of the crosswind yaw angle on the vehicle's aerodynamic characteristics. Taking the Xihoumen Bridge as the engineering background, Yang *et al.*[32] investigated the wind speed profiles of different lanes through numerical simulation and evaluated the crosswind loads of different vehicle types. On this basis, an optimal scheme for reducing wind resistance was obtained, and an adjustable wind barrier was proposed and used in field practice. Chu *et al.*[33] studied the protective effect of windbreak height and porosity on vehicles in crosswind environment by numerical simulation. The finding suggests that a porous windbreak forest can effectively diminish the lateral force coefficient of the vehicle, and the 2-m-high windbreak forest plus 0.8 m high guardrail can effectively ensure the driving safety of the 3.6-m-high vehicle.

Existing research primarily focuses on the impact of crosswinds on vehicle aerodynamics, particularly at bridges. However, the aerodynamic effects on vehicles in hilly areas and the necessity for wind protection in such environments have been largely overlooked. This study addresses this significant gap by analyzing the variation in aerodynamic load when vehicles pass by hills under crosswind conditions and exploring protective measures.

Utilizing the improved delayed detached eddy simulation (IDDES) turbulence model and porous media model, establish a three-dimensional computational fluid dynamics (CFD) numerical model for the hill–embankment–wind barrier–vehicle–air system. The accuracy of the numerical simulation is validated through field vehicle tests and wind tunnel experiments. This study analyzed the characteristics of the aerodynamic performance of the vehicle when passing by a hill under three different conditions (without wind barrier, solid wind barrier, and ventilation wind barrier). Section II provides a detailed description of the numerical simulation model and the solution method. Section III verifies the correctness of the numerical simulation from different perspectives. Section IV elucidates the analysis of aerodynamic loads and the flow field structure of the vehicle under different windproof measures. Section V concludes the main findings.

II. CFD MODEL

A. Turbulence model

Improved delayed detached eddy simulation (IDDES) is a hybrid turbulence model that integrates both Reynolds-averaged Navier–Stokes (RANS) and large eddy simulation (LES) methods. This approach leverages the RANS method for flow field simulation in regions close to walls, such as the surface of a vehicle, while employing the LES method in regions far from walls where turbulence is fully developed. This combination allows the IDDES model to inherit the computational efficiency of the RANS method while also possessing the high-resolution characteristics of the LES method.[34,35]

The selection of IDDES as the main tool for this research was primarily influenced by two factors. First, it demonstrates significant advantages in simulating complex flow field structures, particularly in handling separated flows and unsteady flows under high Reynolds number conditions, where IDDES can provide more accurate predictive results and a more detailed analysis of flow structures. Second, previous studies have applied this method to simulate high-speed driving conditions of vehicles in crosswind environments.[36] Based on this, this study employs the IDDES turbulence model based on the shear stress transport k-ω two-equation (SST k-ω) model for simulation. The formula for calculating IDDES is as follows:[37]

$$l_{hyb} = f_{hyb}(1+f_e)\frac{\sqrt{k}}{C_\mu \omega} + (1-f_{hyb})C_{DES}\Delta, \tag{1}$$

$$f_{hyb} = \max\{(1-f_{dt}), f_{step}\}, \tag{2}$$

$$f_{dt} = 1 - \tanh\left[\left(20\frac{\nu_t}{\kappa^2 d_w^2\sqrt{0.5(\mathbf{S}^2+\mathbf{\Omega}^2)}}\right)^3\right], \tag{3}$$

where f_e and f_{hyb} represent the lifting function and mixing function; ω represents the specific dissipation rate; k represents the turbulent kinetic energy; Δ represents the sublattice length scale; f_{dt} represents the delay function of DDES; f_{step} represents a function that provides a fast switching from RANS to LES at the depth of the boundary layer; ν_t represents the vortex viscosity; κ represents the Von Karmen constant; d_w represents the distance from the wall; and $\mathbf{S}$ and $\mathbf{\Omega}$ represent the strain rate and rotation rate tensor normalized by the turbulence timescale, respectively.

B. Porous media model

In this study, a porous medium model is employed to simulate the ventilation wind barrier. The specific implementation method involves adding a source term to the momentum equation, which represents momentum consumption. This term includes both the viscous loss term and the inertial loss term.[38] However, when the crosswind traverses the wind barrier vertically, the velocities in the two directions perpendicular to the flow almost approach zero. As a result, only the momentum loss in the direction perpendicular to the wind barrier is taken into account. Furthermore, due to the high permeability coefficient in the direction perpendicular to the wind barrier, the viscous loss term can be neglected, and only the inertial loss term is considered. The calculation formulas for the viscous loss term and the inertial loss term in the porous medium are as follows, where the first term is the viscous loss term and the second term is the inertial loss term[39,40]

$$S_i = -\left(\frac{\mu}{\alpha} v_i + C_2 \frac{1}{2} \rho |v| v_i\right), \tag{4}$$

where μ represents the dynamic viscosity of air; α is the permeability coefficient; $|v|$ and ρ represent the velocity and density of air; the viscous resistance coefficient $C_1 = 1/\alpha$, taken as 2.111×10^8; and C_2 represents the inertial resistance coefficient, which is usually determined by an empirical formula. The calculation formula is as follows:[41]

$$C_2 = \frac{1}{C^2} \frac{(S_t/S_o)^2 - 1}{t_p}, \tag{5}$$

where C is the coefficient affected by the Reynolds number (Re) and t_p/D_p, usually 0.98 (t_p and D_p are the thickness and diameter of the ventilation plate); S_t and S_o represent the total area of the porous media plate and open area of the porous media plate, when the opening rate is 50%, S_t/S_o=2. Therefore, C_2 is taken as 31.24.

C. Geometric model and boundary conditions

Figure 2 illustrates the geometric model of the vehicle employed in the numerical simulation. The vehicle is based on a commonly used Santana car, scaled at a ratio of 1:1. Small details such as the wheel hub, door handle, and intake grille are simplified, and the vehicle's bottom is smoothed. The vehicle dimensions are as follows: length (L) =4.475 m, width (W)=1.706 m, height (H)=1.469 m. Considering the convenience of meshing, the tire's bottom is positioned 0.01 m above the ground.

Figure 3 exhibits the geometric model employed in the numerical simulation. The global computing domain is simulated as a cuboid, measuring 44.7L in length, 58.62W in width, and 34H in height. The road is designed based on a highway test section, featuring a two-way, four-lane configuration separated by a central separation belt with a width of 0.59W. Each single road surface has a width of 3.52W. The embankment has a height of 1.36H, a width of 3.52W, and a slope ratio of 1:3. The topography of the site was scanned using a drone equipped with a 20 × 10^6-pixel sensor, and the scanned data were processed using Rhino 7 software to obtain the hill's dimensions: length = 8.2L, width = 5.4W, and height = 2.55H. This study considers three different working conditions: without wind barrier, solid wind barrier, and wind barrier with a ventilation rate of 50%. The wind barrier is positioned at the edge of the road near the hill, with a width of 0.12W and a height of 1.36H. At a distance of 0.44W from the wind barrier's edge, the vehicle drives straight by the hill and wind barrier maintaining a velocity of 100 km/h along the roadway adjacent to the wind barrier.

Figure 3 also illustrates the model's boundary conditions. The inflow surface of the atmospheric domain adopts a velocity-inlet boundary condition, while the top surface utilizes a symmetry boundary condition. The rest of the atmospheric outlet interface employs a pressure-outlet boundary condition, and the ground surface, hill surface, road surface, and vehicle surface adopt a no-slip wall boundary condition. When the wind barrier is a solid wind barrier, the surface boundary condition is configured as a no-slip wall, and when it is a ventilation wind barrier, the boundary condition becomes interface.

D. Grid model and solution settings

The Fluent meshing technique is being utilized to mesh the computational domain in this study, and the grid model primarily consists of Poly-Hexcore body meshes.[42] Figure 4 illustrates the employed grid model. The calculation area is divided into two regions: the dynamic grid (A) and the static grid (B). The two regional flow fields interact through an Interface. The dynamic grid is subdivided into three areas: the core encryption area (A2) and the front and rear layer areas (A1 and A3) of the vehicle. Area A2 encompasses the vehicle and the surrounding air. The vehicle's surface is mainly composed of regular polygon grids with a size ranging from 1 to 5 mm. A 10-layer boundary layer is established in close proximity to the vehicle body and tire surface. The first layer has a thickness of 0.001 m, gradually expanding outward at a ratio of 1.2 (estimated, $y+<1$). Areas A1 and A3 represent the front and rear ply areas of the vehicle, consisting of hexahedral structured grids measuring 0.25 m. Both the volume grid and surface grid of regions A1, A2, and A3 are assigned a "Rigid" setting. The sliding mesh approach is employed to simulate the vehicle's motion. A user-defined function (UDF) is utilized to simulate the forward motion of the vehicle at a speed of 100 km/h for the rigid component.

Poly-Hexcore volume grids are employed to populate the static grid regions, which remain static during the calculation. Two layers of dense regions (B1 and B2) are implemented to expand the static grid area progressively from the interior to the exterior, with the grid size at the outermost boundary set approximately to 1 m. Five boundary layers are applied to the surface of the wind barrier and the hill, with the first layer having a thickness of about 0.005 m. The thickness expands outward at a ratio of 1.2. The total number of grid units is estimated to be approximately 47 × 10^6.

The Fluent finite element and the finite volume method (FVM) are used to solve the flow field around the vehicle. The second-order upwind scheme is employed for solving both the time integration and momentum equations. The time step for the simulation is set to 10^{-4} s. Under this time step, the Courant number (CFL) value for over 99% of the grids is less than one, with the maximum CFL value being approximately 1.3. The minimum convergence value of the residual is set to 10^{-6}, and each time step is iterated 30 times.

Numerical simulations are being performed on a supercomputer cluster, which consists of 980 standard computing nodes. Each node is outfitted with two 12-core Intel Xeon processors, each running at a main frequency of 2.5 GHz. The computation time for each model is approximately 70 h. For post-processing tasks, such as the creation of flow field diagrams, a series of workstations is used. These workstations are configured to harness the power of 128 cores and are allocated 256GB of memory.

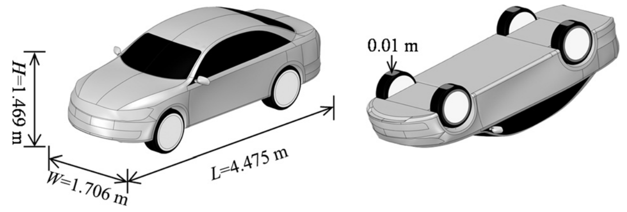

FIG. 2. Geometric model of vehicle.

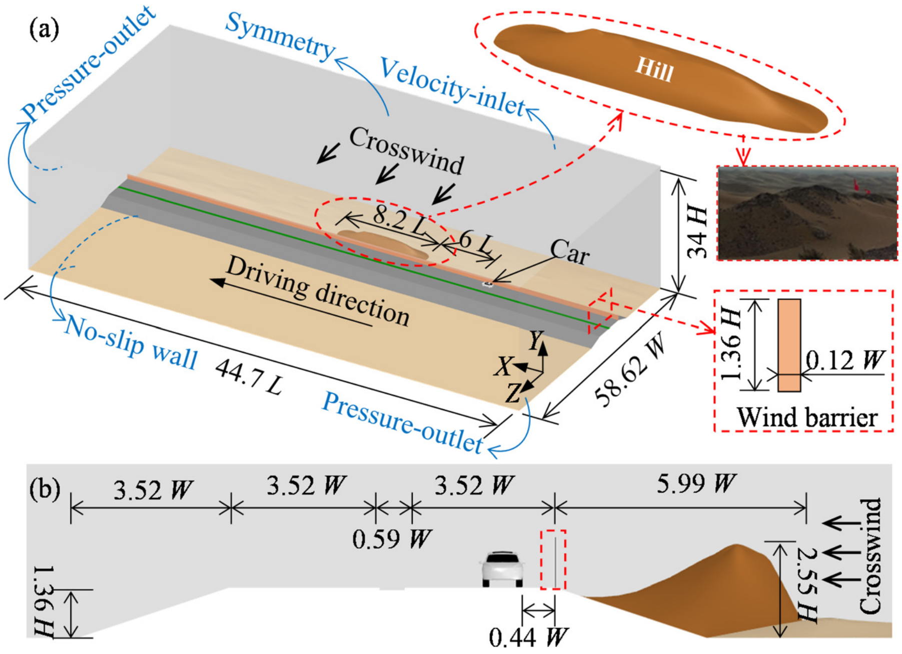

FIG. 3. Geometric model and boundary conditions of numerical simulation: (a) Overall schematic; (b) cross section.

E. Calculation of aerodynamic loads coefficients

When the vehicle operates at high speeds in a crosswind environment, it is subjected to transient aerodynamic loads. Abrupt changes in operating scene can lead to deteriorating aerodynamic behavior, posing a safety threat to the vehicle. The vehicle's aerodynamic loads include drag (F_x), lift (F_y), lateral force (F_z), rolling moment (M_x), yaw moment (M_x), and nodding moment (M_z). Among these, F_y, F_z, M_x, M_x, and M_z have a significant impact on driving safety, potentially resulting in dangerous behaviors. F_x is directly related to the fuel economy of the vehicle.[43] In the numerical simulation, the grid unit on the vehicle body surface is considered as the calculation unit surface, and a corresponding user-defined function (UDF) program is compiled to solve the transient solution of each grid unit on the vehicle body surface. Finally, time–history data of diverse aerodynamic loads on the vehicle are obtained for further analysis. To better analyze and compare the variation law of vehicle aerodynamic load, we use Eqs. (6)–(11) to dimensionless F_z, M_x, and M_y

$$C_x = \frac{2F_x}{V^2 S_c \rho}, \tag{6}$$

$$C_y = \frac{2F_y}{V^2 S_c \rho}, \tag{7}$$

$$C_z = \frac{2F_z}{V^2 S_c \rho}, \tag{8}$$

$$C_{mx} = \frac{2M_x}{V^2 S_c H_c \rho}, \tag{9}$$

$$C_{my} = \frac{2M_y}{V^2 S_c H_c \rho}, \tag{10}$$

$$C_{mz} = \frac{2M_z}{V^2 S_c H_c \rho}, \tag{11}$$

where V represents the vehicle speed; ρ represents the air density; S_c and H_c represent the side area and height of the vehicle; and C_z, C_{mx}, and C_{my} represent the lateral force coefficient, rolling moment coefficient, and yaw moment coefficient, respectively.

III. VERIFICATION

A. Independence verification

The accuracy of aerodynamic load calculation is intricately tied to the dimensions and quantity of grids in the simulation. To verify the

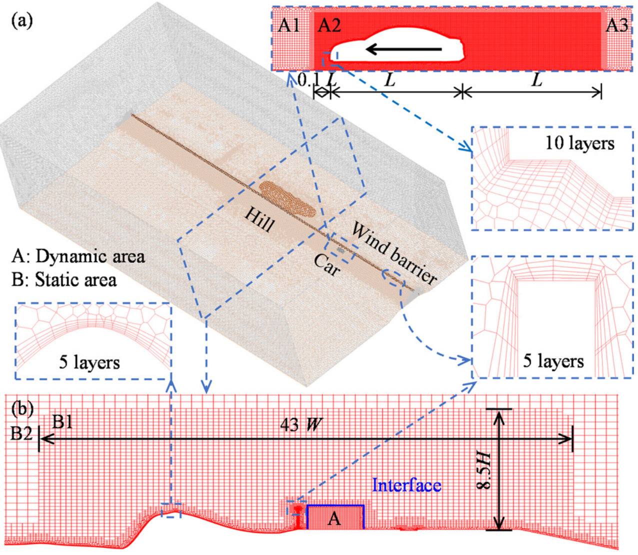

FIG. 4. Grid model: (a) overall model and (b) cross section.

grid independence, keep the thickness and number of the first layer of the outer boundary layer of the vehicle body unchanged and establish coarse, medium, and fine grid models by changing the size of the grid on the vehicle body surface, respectively [as shown in Fig. 5(a)]. The total grid count for the three models is 35×10^6 (coarse grid), 47×10^6 (medium grid), and 59×10^6 (fine grid). The calculation conditions are as follows: the IDDES turbulence model is selected, a steady wind with a constant speed of 20 m/s is oriented along the Z-axis, the vehicle speed is 100 km/h, there is no wind barrier on the side of the road, and other solution settings are consistent with Sec. II. Furthermore, a time step independence verification is also performed. The time steps considered are 2×10^{-4}, 10^{-4}, and 5×10^{-5} s, with each simulation running for a total of 2.8 s.

The time history curves of C_z when the vehicle passes by the hill are taken as the monitoring indexes. Figures 5(b) and 5(c) show the comparison of the monitoring indexes under different grid sizes and time steps. The results demonstrate a high level of agreement between the calculations for the model with 47×10^6 gird elements and the model with 59×10^6 grid elements. The disparity in the peak value of C_z is minimal, at just 1.6%. Alterations in the time step have a negligible effect on the C_z time history curve, mainly influencing the magnitude of its peaks. At a time step of 2×10^{-4} s, the positive and negative peak values of C_z were reduced by 3.99% and 7.36%, respectively, compared to a time step of 10^{-4} s. Conversely, at 5×10^{-5} s, these values increased by 2.01% and 3.68%, respectively. This suggests that as the time step diminishes, the amplitude of C_z variations stabilizes. Hence, the selection of a model comprising 47×10^6 grid cells and a time step of 10^{-4} s is deemed reasonable.

B. Verification of aerodynamic loads coefficients

To verify the precision of the numerical simulation results concerning the aerodynamic load on the vehicle, a corresponding numerical model was established, based on the wind tunnel test conducted by Wang *et al.*[18] As illustrated in Fig. 6, the numerical simulation aligns with the wind tunnel experiments in scale ratio, computational domain dimensions, vehicle model specifications, and boundary conditions. The computational domain measures 17 m in length, 3 m in width, and 2.5 m in height. The vehicle model is scaled down to a 1:3 ratio. The incoming wind velocity is configured at 30 m/s, and the vehicle model is rotated to simulate various yaw angles, stepping through every 3° from −9° to 9°. The vehicle remained stationary. The inflow boundary of the computational domain is set as velocity-inlet, the outflow as pressure-outlet, and the perimeter as well as the vehicle surface are designated as no-slip wall. The turbulence model and the meshing method are consistent with those in Sec. II. However, due to factors such as wall roughness, experimental apparatus, and temperature gradients, wind tunnel tests cannot fully emulate uniform wind conditions, resulting in minor discrepancies when compared to numerical simulations.

Using the average drag and lateral force coefficients of the vehicle as benchmarks, Fig. 7 presents a comparison between the outcomes derived from numerical simulation and those from wind tunnel tests, with the discrepancies highlighted on the graph. It can be observed that the vehicle's drag coefficient and lateral force coefficient calculated through numerical simulation align well with the wind tunnel test results, with a deviation within 5%. Notably, the lateral force coefficient exhibits the closest agreement. The slight deviation could be attributed to inconsistencies in the roughness of the numerical model and experimental model or variations in ambient temperature and humidity.

To further verify the applicability of the numerical simulation method under different wind speeds and vehicle types, a numerical simulation model of a moving vehicle consistent with the wind tunnel tests conducted by Xiang *et al.*[44] has been established. As shown in Fig. 8, the dimensions of the numerical simulation domain are 36 m in length, 22.5 m in width, and 4.5 m in height. The bridge model is simplified to a simply supported beam model, while the vehicle model is simplified to a rectangular prism with dimensions of 0.14 m in length, 0.125 m in width, and 0.52 m in height. The angle between the vehicle speed and the wind direction (β) is also defined in the figure. The boundary conditions are set the same as in Fig. 6, and the turbulence model and the meshing method are consistent with those described in Sec. II. Figure 9 displays the time history curves of the vehicle's lift and lateral forces at a wind speed of 10 m/s and $\beta = 60°$, as well as the variation of the vehicle's lateral force at wind speeds of 8 m/s and 10 m/s with $\beta = 55°$.

Analysis of Fig. 9 indicates that the aerodynamic load time history curves obtained from wind tunnel tests are more disordered, while the numerical simulation results show a more regular pattern. Nonetheless, the difference between the average values of the two is relatively small, with the average difference in lift and lateral forces being 6.53% and 7.75%, respectively. At wind speeds of 8 and 10 m/s, the difference in the average lateral force coefficient is 3.03% and 4.64%, respectively. These differences may be due to the difficulty in maintaining a completely consistent vehicle speed during the wind test and some fluctuations in the crosswind. Given the negligible difference, the numerical simulation method used in this study yields precise predictions for the aerodynamic load on the vehicle.

C. Field experimental verification

To further verify the accuracy of the wind speed and pressure simulation results in this study, a series of field experiments were conducted on a highway test section, as depicted Fig. 10. The field experimental site is a two-way, four-lane road segment without wind barriers alongside the road and no crosswinds during the experiment. A Santana sedan is used for the experiment, traveling at a speed of 60 km/h. The wind speed sensor, a Gill Wind Master Pro ultrasonic anemometer, is positioned on the shoulder at a height of 1.2 m above the ground, with a range of 0–65 m/s, an accuracy of 0.01 m/s, and a sampling frequency of 300 Hz. The pressure sensors, which are micro-differential pressure sensors, are fixed on the passenger side door handle and on the wind speed sensor, with a range of −1600–1600 Pa, an accuracy of 0.5% FS, and a sampling frequency of 1000 Hz. The numerical simulation accurately replicates the conditions of the field experiment on a 1:1 scale.

Figure 11 illustrates the comparison between the results of numerical simulation and field measurements. The field measurement data were averaged based on the results of ten repeated experiments, while the numerical simulation data were calculated applying the approach delineated in Sec. II. Analysis of Fig. 11 reveals that, for the wind speed and pressure measuring points on the shoulder, both field measurements and numerical simulations exhibit noticeable fluctuations caused by the vehicle passing by these points. The fluctuation range of wind speed obtained from field measurements and numerical simulations is 1.623 and 1.470 m/s, respectively, with a disparity of

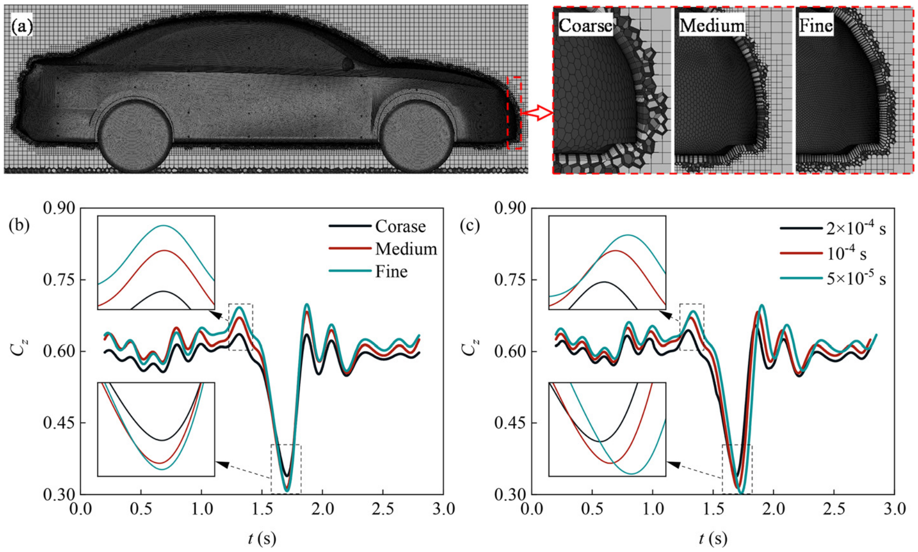

FIG. 5. Independence verification: (a) grid of different thicknesses; (b) grid independence verification; (c) time step independence verification.

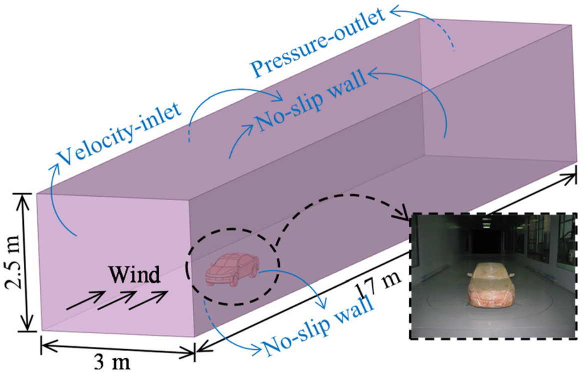

FIG. 6. Comparison of wind tunnel experiment and numerical simulation model.

9.4%. Similarly, the pressure fluctuation ranges are 19.022 and 17.046 Pa, with a difference of 10.4%. Regarding the pressure measuring points on the vehicle's surface, the pressure fluctuates up and down along a horizontal line during the driving process. The average pressure values obtained from field measurements and numerical simulations are −39.1812 Pa and −37.442 Pa, respectively, with a deviation of 4.4%. The disparity between field measurements and numerical simulations can be attributed to the influence of low-speed and continuous environmental wind during the field measurement process, which was not considered in the numerical simulation. Taking all factors into account, it can be concluded that the numerical simulation method employed in this study accurately predicts pressure and wind speed results.

IV. RESULTS AND DISCUSSION

A. Aerodynamic load of the vehicle

To analyze the fluctuations in aerodynamic load coefficients when the vehicle passes by the hill under different windproof measures, Fig. 12 displays the time history curves of the six aerodynamic load coefficients of the vehicle under three conditions: without wind barrier, solid wind barrier, and ventilation wind barrier. The crosswind speed remains constant at 20 m/s across all three conditions, and the velocity of the vehicle is set at 100 km/h. The two vertical dashed lines in the diagram indicate the moments when the front of the vehicle just enters the hill and the tail of the vehicle just makes it out of the hill, respectively, denoted as 1.188 and 2.053 s. The maximum and

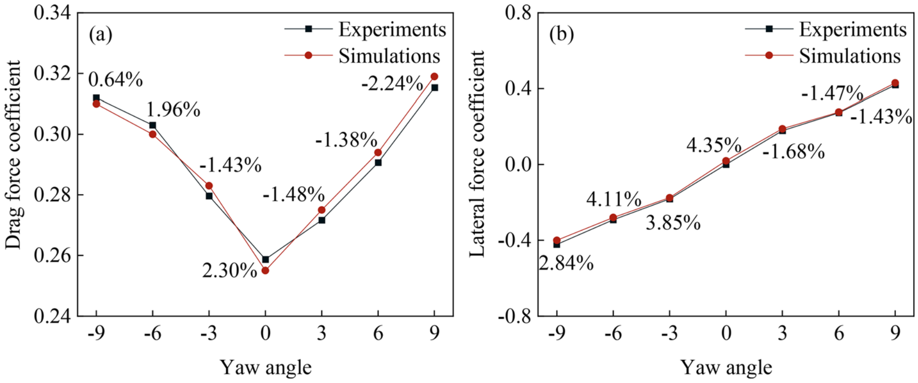

FIG. 7. Comparison of experiment and numerical simulation: (a) drag force coefficient; (b) lateral force coefficient.

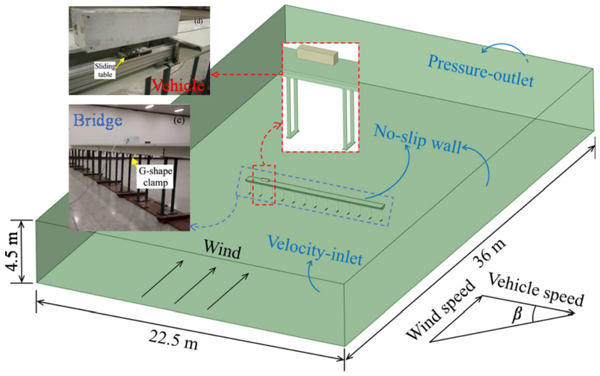

FIG. 8. Comparison of moving vehicle model in wind tunnel tests and numerical simulation model.

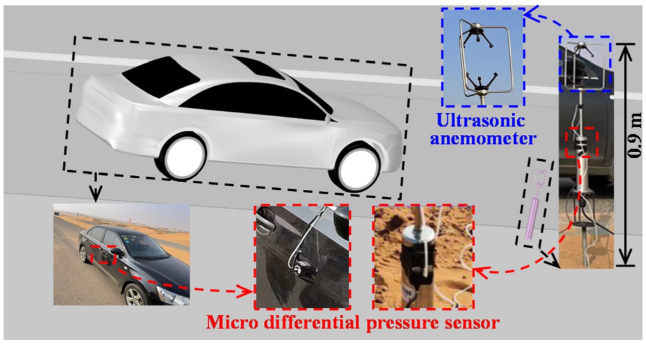

FIG. 10. Schematic layout of pressure and wind speed measurement points on site.

minimum values of the aerodynamic load coefficients are also marked on the graph.

From the analysis of Fig. 12, it can be concluded that when the vehicle travels smoothly on the flat section with crosswinds, all the aerodynamic load coefficients fluctuate at a constant value. However, upon entering the hill section, the aerodynamic load coefficients exhibit more violent fluctuations with greater complexity and range than those observed in the flat section, indicating a reduction in vehicle driving stability and an increase in fuel consumption.

In the condition of without wind barrier, C_y, C_z, and C_{my} initially experience sharp decreases followed by sharp increases, while C_x, C_{mx}, and C_{mz} exhibit more violent fluctuations, characterized by multiple dramatic increases and decreases. The pattern of variation in aerodynamic load coefficients under the ventilation wind barrier is similar to that without wind barrier, but the peak values and variation ranges of aerodynamic load coefficients are significantly smaller. For instance, the maximum and minimum values of C_z under the ventilation wind barrier are 0.233 and 0.041, respectively, representing a 65.89% and 69.40% reduction compared to the values without wind barrier.

However, the aerodynamic load coefficients under solid wind barrier conditions display significant differences from those without wind barrier. In the flat section, C_z and C_{my} exhibit contrasting trends under the solid wind barrier, albeit with smaller magnitudes. Specifically, the average C_z value is -0.212, a 65% reduction in absolute value compared to the condition without a wind barrier. In the hill section, the aerodynamic loads experience multiple cycles of rise and fall, with the most pronounced amplitudes. For instance, C_z starts with an increase, followed by a decrease, and then another rise. The minimum value of the aerodynamic load coefficients occurs when the vehicle is at the midpoint of the hill.

To quantitatively describe the variation amplitude of aerodynamic coefficients under different wind protection measures and to assess the vehicle's driving stability and fuel economy, Fig. 13 showcases the amplitude of variation and standard deviation for the aerodynamic load coefficients during vehicle operations on both flat section and the hill section. To facilitate comparison, all values are normalized by the corresponding data from the flat section without wind barrier, where the values of the flat section are all set to one.

Analysis from Fig. 13 reveals that when the vehicle is driving in the hill section, the standard deviation and variation amplitude of the aerodynamic loads on the vehicle are significantly higher than those on flat ground, with the most pronounced increase under the solid wind barrier condition. This indicates that the vehicle's stability is lower and fuel consumption is higher when driving on hill sections. Specifically, ΔC_x, ΔC_y, ΔC_z, ΔC_{mx}, ΔC_{my}, and ΔC_{mz} in the hill section without wind barrier are 2.79, 4.42, 5.18, 3.73, 4.45, and 2.73 times that of the corresponding values in the flat section, respectively. Similarly, σC_x, σC_y, σC_z, σC_{mx}, σC_{my}, and σC_{mz} in the hill section are 2.25, 4.82, 5.88, 3.09, 5.04, and 2.98 times that of the corresponding values in the flat section, respectively.

Furthermore, the fluctuation amplitude of the aerodynamic load coefficients is the greatest under the solid wind barrier, followed by without wind barrier condition, and the least under the ventilation wind barrier. This suggests that setting up wind barriers with a certain

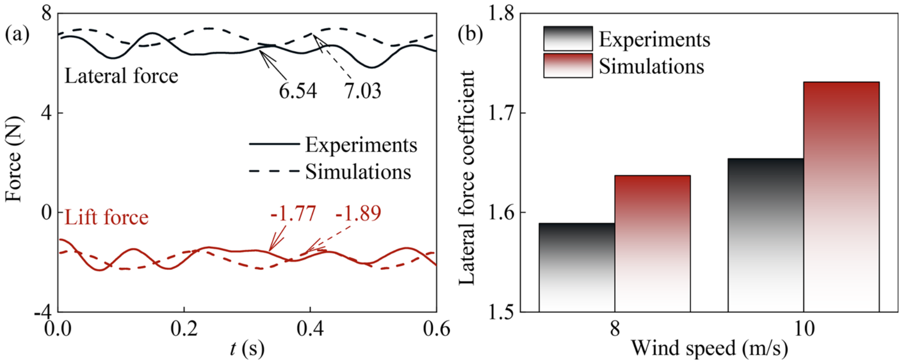

FIG. 9. Comparison between the moving vehicle model in wind tunnel tests and numerical simulation results: (a) time history curves; (b) different wind speeds.

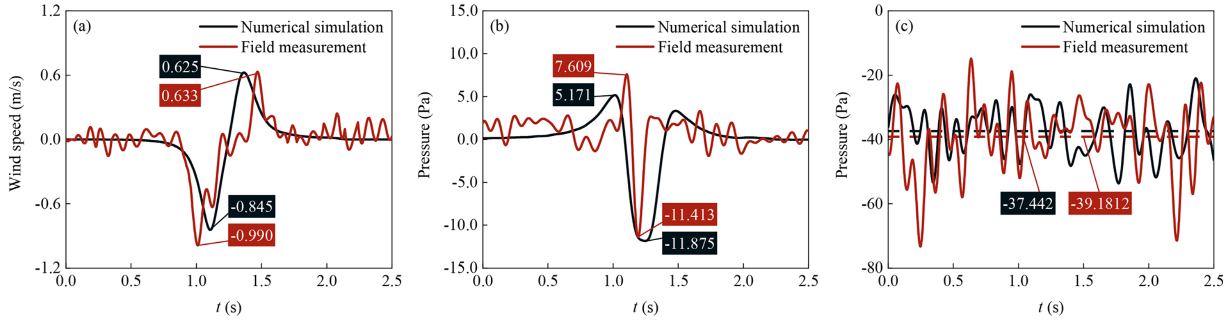

FIG. 11. Comparison between field measurements and numerical simulation results: (a) wind speed at the shoulder; (b) pressure at the shoulder; and (c) vehicle surface pressure.

ventilation rate along the roadside can better mitigate the sudden changes in vehicle aerodynamic forces, thereby improving vehicle driving stability. Notably, the reduction in drag is significant, which can substantially decrease fuel consumption. Taking the hill section as an example, the increase in C_x and C_{mz} is more pronounced. Under the solid wind barrier, ΔC_x, ΔC_y, ΔC_z, ΔC_{mx}, ΔC_{my}, and ΔC_{mz} are 3.48, 1.61, 2.26, 0.95, 1.21, and 3.88 times that without wind barrier, and 3.63, 2.16, 4.34, 2.93, 2.00, and 3.21 times that under the ventilation wind barrier.

Given the effectiveness of ventilation wind barriers in mitigating sudden changes in aerodynamic loads on vehicles, the ventilation wind barrier scenario was selected for analyzing the variation patterns of aerodynamic loads on vehicles under different speeds and crosswind speeds. Figures 14 and 15 present the fitted curves of the variation amplitude of aerodynamic load coefficients for vehicles in the hill section and flat section as a function of vehicle speed and crosswind speed.

Analysis of Figs. 14 and 15 reveals that with the increase in vehicle speed and crosswind speed, the variation amplitude of aerodynamic loads on vehicles in both flat and hill sections shows varying degrees of increase. Notably, vehicle speed has the most significant impact on ΔC_{mx}; when the speed increases from 80 to 120 km/h, the increase in ΔC_{mx} in the hill section is as high as 109.76%, while in the flat section, it increases by 82.58%. Crosswind speed has the most significant impact on ΔC_x; when the wind speed increases from 15 to 25 m/s, ΔC_x increases by 303.03% in the hill section and by 260.67% in the flat section. This also indicates that under the same conditions, the increase in aerodynamic loads on vehicles in the hill section exceeds that in the flat section. As shown in Eq. (R1), linear functions can quantitatively describe the relationship between the variation amplitude of

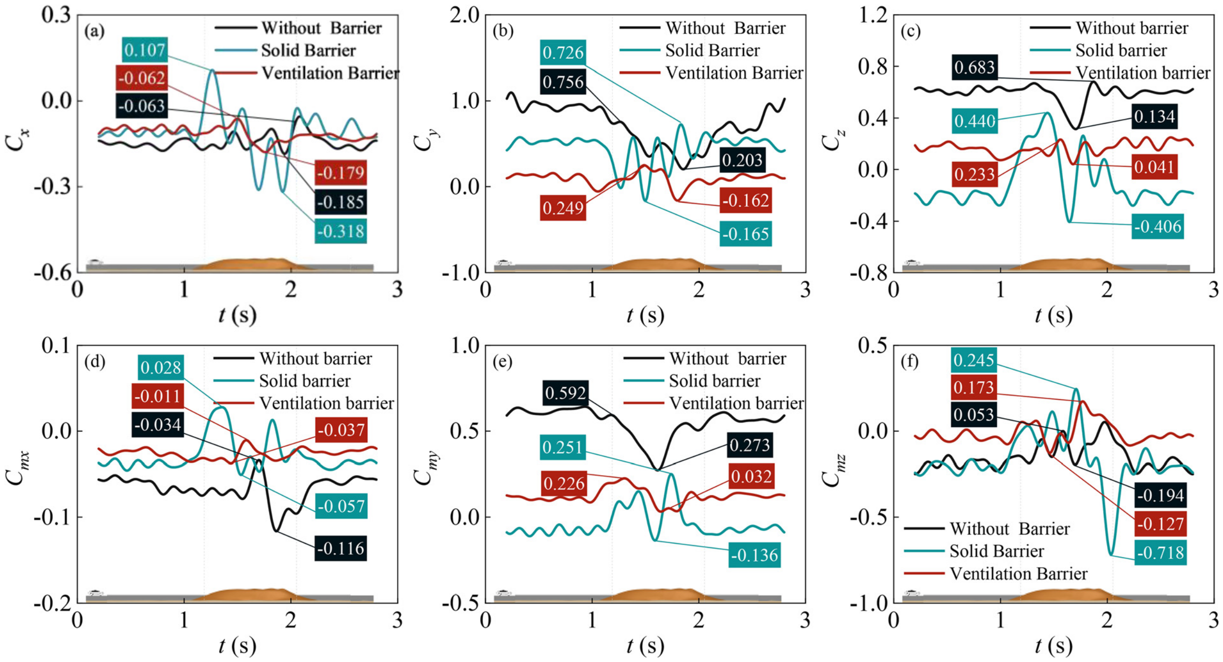

FIG. 12. Time–history curve of aerodynamics loads coefficients: (a) C_x; (b) C_y; (c) C_z; (d) C_{mx}; (e) C_{my}; and (f) C_{mz}.

aerodynamic loads and both vehicle speed and wind speed, with R^2 values all exceeding 0.9, indicating that the linear functions can adequately describe this relationship. The relevant parameters in the fitting functions are shown in Figs. 14 and 15.

$$\Delta C_{ij} = a_{ij}u + b_{ij}, \tag{12}$$

where ΔC_{ij} represents the variation amplitude of the aerodynamic load; a_{ij} and b_{ij} represent the fitting parameters, where $i = 1$–6 corresponds to the vehicle's C_x, C_y, C_z, C_{mx}, C_{my}, and C_{mz}; and $j = 1$ and 2 correspond to the variation amplitude of aerodynamic loads in the flat section and the hill section, respectively.

B. Power spectral density

The power spectral density (PSD) of the aerodynamic load on the vehicle body is commonly used to analyze the distribution of impact loads on the vehicle body in the frequency domain.[45] Figure 16 illustrates the PSD of the F_x, F_y, F_z, M_x, M_y, and M_z obtained through fast Fourier transform (FFT) under different windproof measures.

From the analysis of Fig. 16, it indicates that the PSD of aerodynamic loads on vehicles passing by the hill exhibits notable variations under different windproof measures. The PSD frequencies across all conditions range from 0.38 to 500 Hz, each characterized by a predominant frequency. For scenarios without wind barrier and with ventilation wind barrier, the PSD of aerodynamic loads trends upward initially and then declines with the rise in frequency, with the main frequencies being 1.14 and 2.31 Hz, respectively. Conversely, under solid wind barrier, the PSD of aerodynamic loads consistently diminishes as frequency increases, with a main frequency of 0.38 Hz.

Additionally, the PSD peak values for vehicle aerodynamic loads under different windproof measures show that the solid wind barrier has the highest peak value, followed by the scenario without a barrier, and the ventilation barrier has the lowest. The PSD peak value variation is most pronounced for F_x and least for F_y under different windproof measures. Specifically, under the solid wind barrier, the PSD peak values for F_x, F_y, F_z, M_x, M_y, and M_z are 1.49 (4.52), 1.31 (2.58), 2.12 (3.41), 1.59 (2.95), 1.79 (2.46), and 1.91 (2.58) times those observed without barrier (with ventilation barrier), respectively. This phenomenon suggests that the vehicle's aerodynamic load frequency is lowest and its energy is highest with the solid wind barrier, whereas the aerodynamic load frequency is highest and its energy is lowest with the ventilation barrier.

C. Surface pressure of the vehicle

To analyze the variation in surface pressure as the vehicle passes by a hill with different windproof measures, Fig. 17 illustrates the pressure time history curves for points on both the windward side (1#) and leeward side (2#) of the vehicle. The average pressure value during flat section driving and the maximum and minimum values during hill section driving are marked.

As observed from Fig. 17, there is a significant variation in surface pressure for points located windward (1#) and leeward (2#) of the vehicle under different windproof measures. In Fig. 17(b), when the vehicle enters the hill, for the windward side, the surface pressure of vehicle without wind barrier experiences several processes of rising and falling. The measuring point remains under positive pressure for most of the time, with only a small portion of negative pressure when the vehicle is driving in the middle of the hill. The average pressure during flat section driving is 241 Pa, and the maximum and minimum pressures during hill section driving are 373 Pa and −133 Pa, respectively. Upon the vehicle traversing the solid wind barrier, the surface pressure also undergoes several rising and falling processes, but the measuring points are all subjected to negative pressure. The average pressure during flat section driving is −441 Pa, and the maximum and minimum pressures during hill section driving are −89 and −746 Pa, respectively. On the other hand, upon the vehicle traversing the solid wind barrier, the surface pressure first decreases and then increases. The average pressure during flat section driving is −254 Pa, and the maximum and minimum pressures during hill section driving are −206 and −352 Pa, respectively.

In Fig. 17(c), when the vehicle enters the hill, the leeward-side measuring point without wind barrier experiences an initial increase followed by a decrease in pressure. The average pressure during flat section driving is −562 Pa, and the maximum and minimum pressures during hill section driving are −95 and −527 Pa, respectively. The pressure under the solid wind barrier condition also undergoes multiple processes of increasing and decreasing pressure, with the average pressure during flat section driving is −435 Pa, and the maximum and minimum pressures during hill section driving are −128 and −742 Pa, respectively. Conversely, the leeward side measuring point corresponding to the ventilation wind barrier condition experiences a decrease

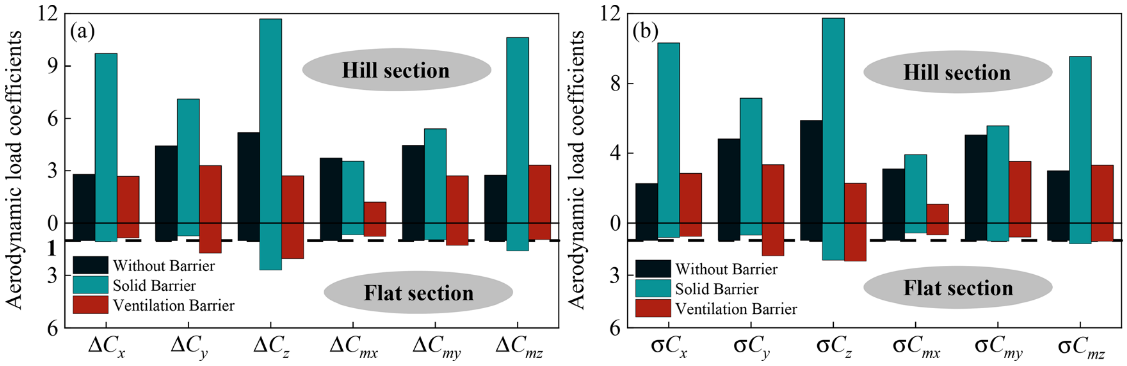

FIG. 13. Normalized aerodynamic loads on the vehicle: (a) amplitude; (b) standard deviation.

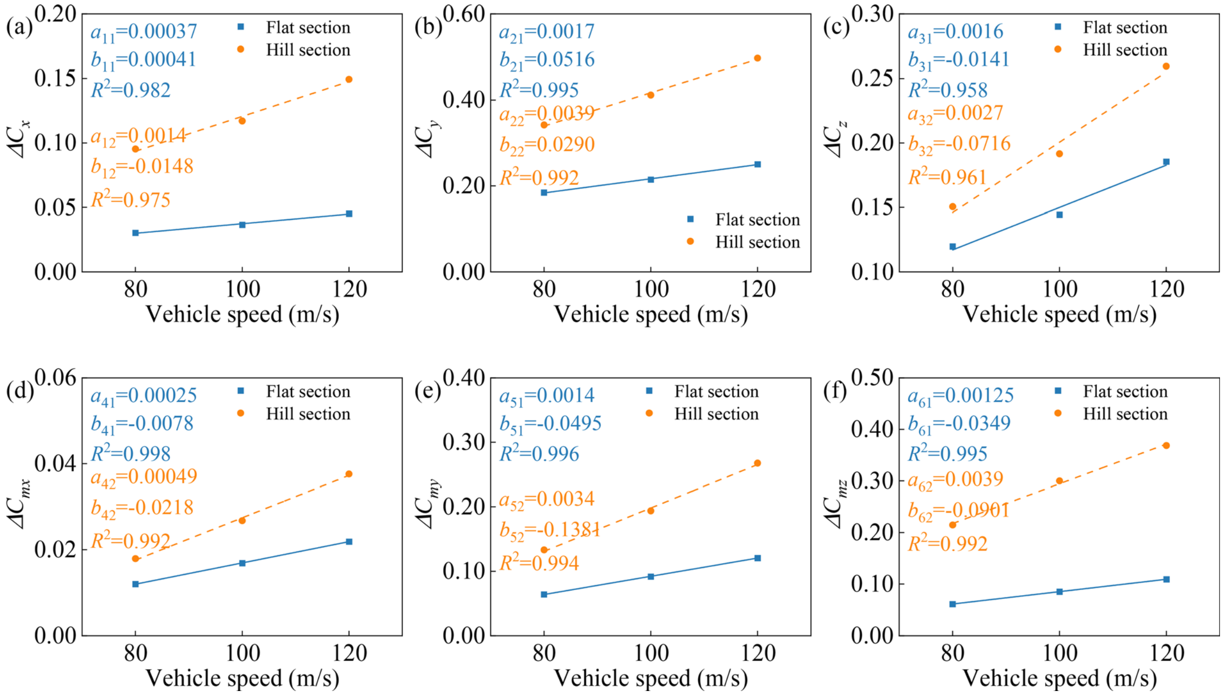

FIG. 14. Fitted curves of the variation amplitude of aerodynamic load coefficients with vehicle speed: (a) ΔC_x; (b) ΔC_y; (c) ΔC_z; (d) ΔC_{mx}; (e) ΔC_{my}; and (f) ΔC_{mz}.

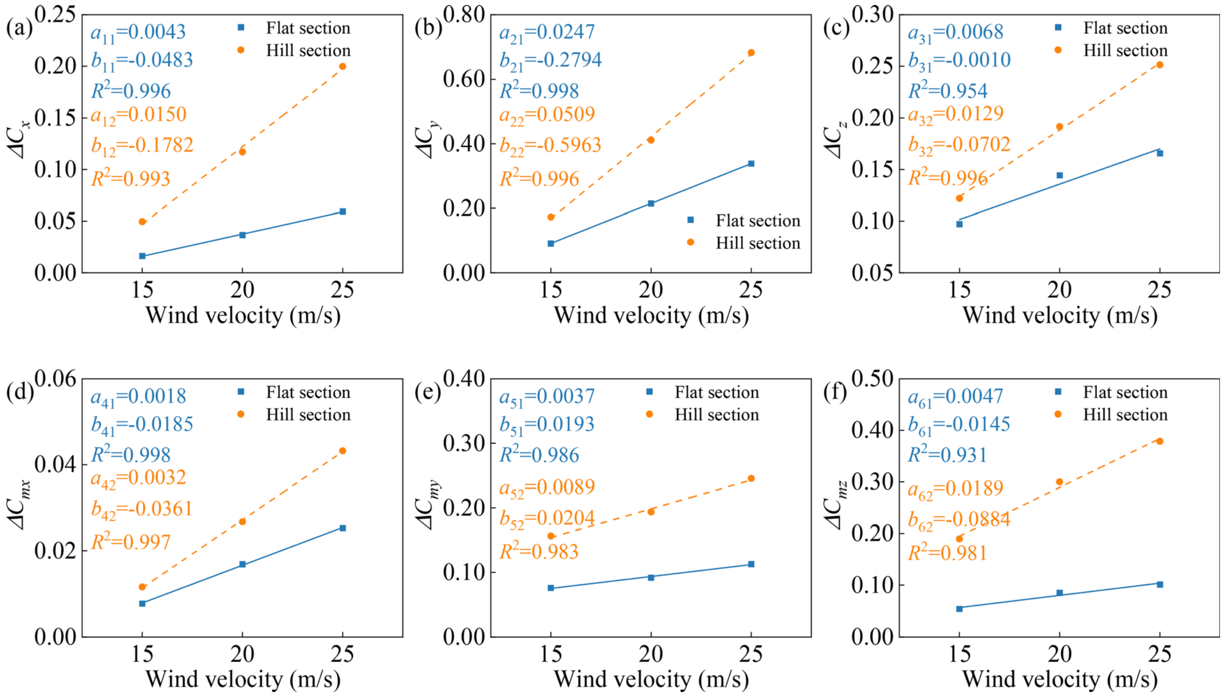

FIG. 15. Fitted curves of the variation amplitude of aerodynamic load coefficients with wind speed: (a) ΔC_x; (b) ΔC_y; (c) ΔC_z; (d) ΔC_{mx}; (e) ΔC_{my}; and (f) ΔC_{mz}.

followed by an increase in pressure, exhibiting an opposite pattern compared to the without wind barrier condition. The average pressure during flat section driving is −261 Pa, and the maximum and minimum pressures during hill section driving are −218 and −430 Pa, respectively. It is worth noting that the variation range of surface pressure on the vehicle body during hill section driving under different windproof measures is much greater than that during flat section driving. Under three different working conditions (without wind barrier, solid wind barrier, and ventilation wind barrier), the measured pressure standard deviations at 1# measurement point in the hill section are 95.5, 166.4, and 39.1. These values are 12.5, 15.9, and 2.3 times greater than those in the flat section. For the 2# measurement point, the standard deviations of pressure are 104.9, 144.3, and 56.2, respectively, which are 2.6, 3.5, and 2.7 times greater than those in the flat section.

When the vehicle traverses the solid wind barrier, pressure fluctuations on both the windward and leeward sides are significantly higher compared to conditions without a wind barrier and with a ventilation wind barrier. In contrast to the solid wind barrier scenario, the average pressure values on the windward and leeward sides decrease by 46% and 29%, respectively, in the condition of without wind barrier. Similarly, the variation ranges in the hill section also show reductions of 23% and 30%, respectively. Under conditions with a ventilation wind barrier in the flat section, the absolute values of average pressure experience a decrease in 42% and 40%, and the variation ranges in the hill section witness substantial reductions of 78% and 66%, respectively.

Figures 18–20 display the pressure cloud diagrams of the vehicle's windward side, leeward side, top, and bottom at four critical moments during the vehicle's passage by the hill under different windproof measures. Additionally, the diagrams indicate the average pressure on each surface of the vehicle. These moments correspond to $t = 1.20$, 1.35, 1.70, and 2.05 s, representing the moments when the vehicle has not yet entered the hill, half of the vehicle body has entered the hill, the vehicle is at the midpoint of the hill, and half of the vehicle body has exited the hill, as depicted in Fig. 18(e).

Analysis of Figs. 18–20 reveals that there is a significant change in the pressure distribution across the vehicle's surface as it passes by the hill without wind barrier. During the flat section (t_1 moment), the rear wheel and its front area on the windward side of the vehicle experience positive pressure, while only a part of the area behind the rear wheel is subjected to negative pressure, and the average pressure is about 409 Pa. On the leeward side, the pressure distribution is opposite to that on the windward side, with most of the area subjected to negative pressure, and the average pressure is about −486 Pa. The vehicle is subjected to a large lateral force during this time. It is noteworthy that a positive high-pressure zone is present on the leeward side of both the front and rear wheels at the vehicle's bottom. This implies that the wheels experience increased pressure, resulting in substantial lateral forces. When the vehicle enters the hill section (t_2 moment), the surface pressure distribution diagram is similar to that of the t_1 moment, but the absolute values of pressure have slightly decreased. The pressures on the windward side, leeward side, top, bottom, front, and rear of the vehicle have decreased by 1.47%, 15.84%, 9.92%, 34.30%, 5.75%, and 24.13%, respectively. This similarity explains the relatively small magnitude of change in aerodynamic load as the vehicle gradually ascends from flat ground to the hill. As the vehicle completely enters the hill section (t_3 moment), the high-pressure zone primarily concentrates at the front section of the vehicle, which is about 158 Pa. However, positive pressure is additionally noted in proximity to the

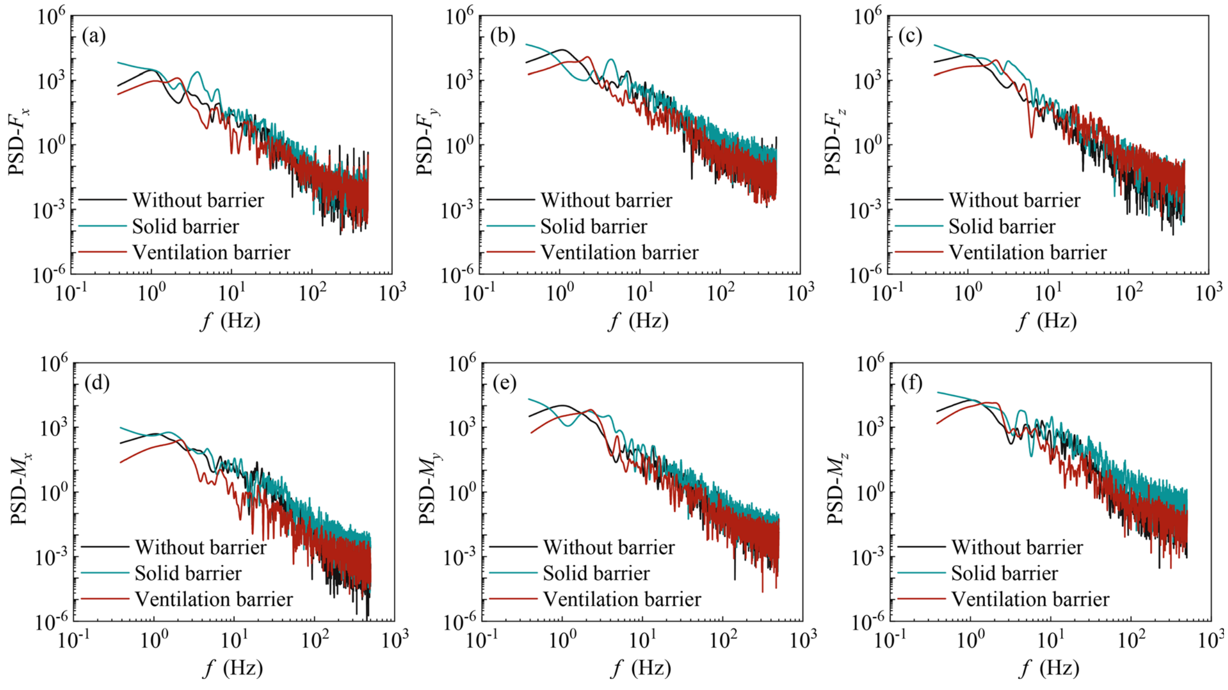

FIG. 16. PSD of aerodynamic load: (a) F_x; (b) F_y; (c) F_z; (d) M_x; (e) M_y; and (f) M_z.

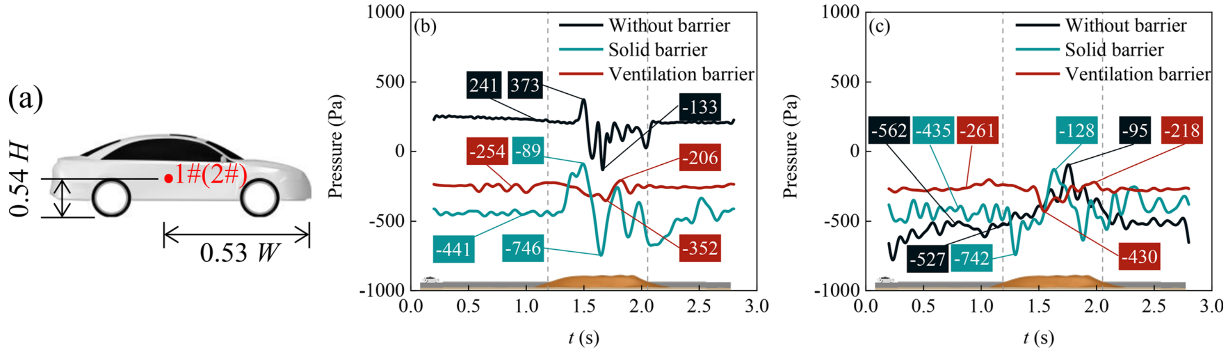

FIG. 17. Vehicle surface pressure time history curves: (a) schematic location of measurement points; (b) windward side (1#); and (c) leeward side (2#).

rear door, the rear wheel on the leeward side, and the underside of the vehicle. This contributes to a reduction in the vehicle's lateral force and an augmentation of the yaw moment. When the vehicle drives out of the hill section (t_4 moment), the positive pressure region on the rear side of the leeward side tends to diminish, resulting in a subtle increment in the lateral force.

Under the condition of solid wind barrier, the distribution pattern of surface pressure on the vehicle changes more significantly over time. During the flat section (t_1 moment), compared to the leeward side, the windward side of the vehicle experiences greater negative pressure. This distribution is opposite when compared to the condition of without wind barrier, resulting in the vehicle experiencing a negative lateral force. The average pressures on the windward side, leeward side, top, bottom, front, and rear of the vehicle are −180, 85, −292, −272, −155, and −279 Pa, respectively. When the vehicle enters the hill section (t_2 moment), the pressures on the leeward side and the top of the vehicle have significantly decreased, with average pressures being −528 and −604 Pa, respectively, and the absolute value of the negative pressure on the leeward side is greater than that on the windward side. Consequently, the direction of the lateral force changes from negative to positive. As the vehicle completely enters the hill section (t_3 moment), the absolute value of negative pressure on the windward side of the vehicle is higher than that on the leeward side, with average pressures being −487 and −336 Pa, respectively. Additionally, there is a significant increase in pressure on the front part, with an average value reaching 130 Pa. This reversal in pressure leads to a change in the direction of the lateral force. When the vehicle drives out of the hill section (t_4 moment), the windward side continues to experience a significant negative pressure (approximately −661 Pa), while the positive pressure region on the leeward side decreases slightly, resulting in a marginal rise in the lateral force.

Under the condition of ventilation wind barrier, the pressure pattern on the vehicle's surface undergoes minimal alterations over time. This phenomenon explains why there is little variation in aerodynamic load when the vehicle traverses the hill. When the vehicle approaches the hill (t_1 and t_2 moment), the pressure on the leeward side of the vehicle is less than that on the windward side, the pressure on the top is less than that on the bottom, and the pressure on the front is less than that on the rear. At t_1 moment, the average pressures on the windward side, leeward side, top, bottom, front, and rear of the vehicle are 119, −243, −386, −223, 204, and −225 Pa, respectively. However, the magnitude of the pressures is significantly smaller compared to the condition of without wind barrier. Consequently, the vehicle experiences a positive lateral force, albeit much smaller than without the wind barrier. As the vehicle completely enters the hill section (t_3 moment), the pressure on both the windward and leeward sides become similar, resulting in a lateral force close to zero. When the vehicle drives out of the hill section (t_4 moment), the positive pressure on the windward side gradually increases, and the lateral force increases.

In summary, when the vehicle passes by a hill under different windproof measures, the pressure distribution on the vehicle body surface undergoes significant changes. For the case of without wind barrier, crosswinds exert direct pressure on the vehicle's surface, leading to substantial aerodynamic loads. The average pressure between the vehicle's opposing surfaces consistently favors one side, with the windward side always exceeding the leeward side in pressure, causing the aerodynamic loads to consistently fluctuate in one direction. For the case of ventilation wind barrier, the change in surface pressure follows a similar pattern as without wind barrier, but with lower pressures. As a result, the aerodynamic load experiences reduced peak values and fluctuation ranges. On the contrary, for the case of solid wind barrier, the average pressure difference between the opposing surfaces of the vehicle is larger, even exhibiting pressure inversion phenomena, leading to the greatest fluctuation in aerodynamic loads.

D. Transient flow field around the vehicle

Figures 21–23 compare the flow field structure near three typical cross sections (the middle of the front wheel, middle of the body, and middle of the rear wheel) of the vehicle at four moments (t_1-t_4) while passing by the hill under different windproof measures. The flow field diagrams are stained with the wind speed in the Z direction, and are dimensionless with the incoming wind speed ($U = 20$ m/s).

Analyzing Figs. 21–23 reveal that: in the condition of without wind barrier, during the flat section (t_1 moment), the crosswind directly affects the vehicle's windward side, leading to the generation of positive pressure. After being hindered by the vehicle body, the crosswind rapidly flows along the top and bottom of the windward side, causing flow separation on the leeward side. Consequently, the leeward side and the vehicle's top are subjected to negative pressure. It is important to note that when the airflow passes by the body, it gets blocked by the wheels, leading to flow around the leeward side of the wheels. This flow creates a positive pressure zone when it acts on the

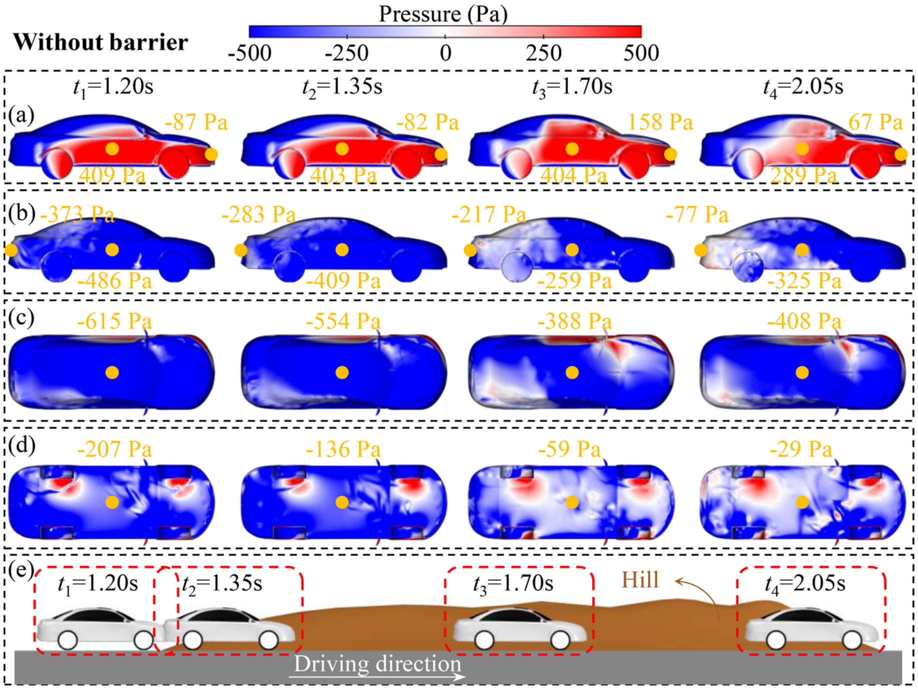

FIG. 18. Surface pressure cloud diagram of the vehicle without wind barrier: (a) windward side; (b) leeward side; (c) top; (d) bottom; and (e) vehicle location schematic.

bottom of the vehicle. When the vehicle enters the hill section (t_2 moment), the flow field structure on the windward side remains mostly unchanged compared to the t_1 moment, with a slightly enlarged vortex structure on the leeward side. As the vehicle completely enters the hill section (t_3 moment), the hill obstructs the crosswind, resulting in a significant reduction in wind speed on the windward side and corresponding reduction in positive pressure. The vortex structure and wind speed on the leeward side decrease, leading to a reduction in negative pressure. When the vehicle drives out of the hill section (t_4 moment), there is a notable increase in crosswind speed on the windward side of the front wheel. Consequently, this elevation in crosswind speed contributes to an increase in surface pressure on the vehicle.

Under the condition of the solid wind barrier, during the flat section (t_1 moment), the crosswind is impeded by the wind barrier, leading to the formation of a large vortex structure on the lee side of the wind barrier. The vehicle's leeward side experiences a crosswind in the $-Z$ direction, leading to positive pressure. After the airflow passes over the vehicle, flow separation occurs on the windward side of the vehicle, forming vortex structures and creating negative pressure. When the

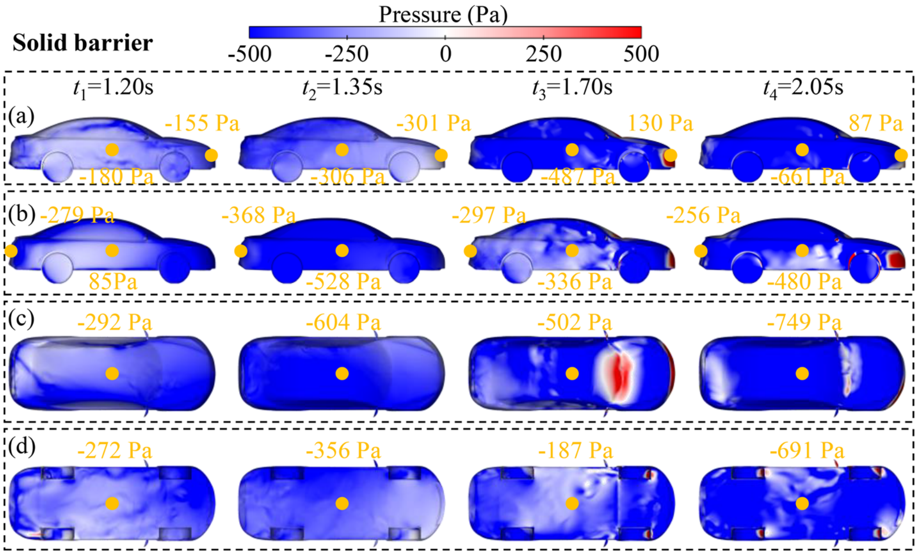

FIG. 19. Surface pressure cloud diagram of the vehicle with the solid wind barrier: (a) windward side; (b) leeward side; (c) top; and (d) bottom.

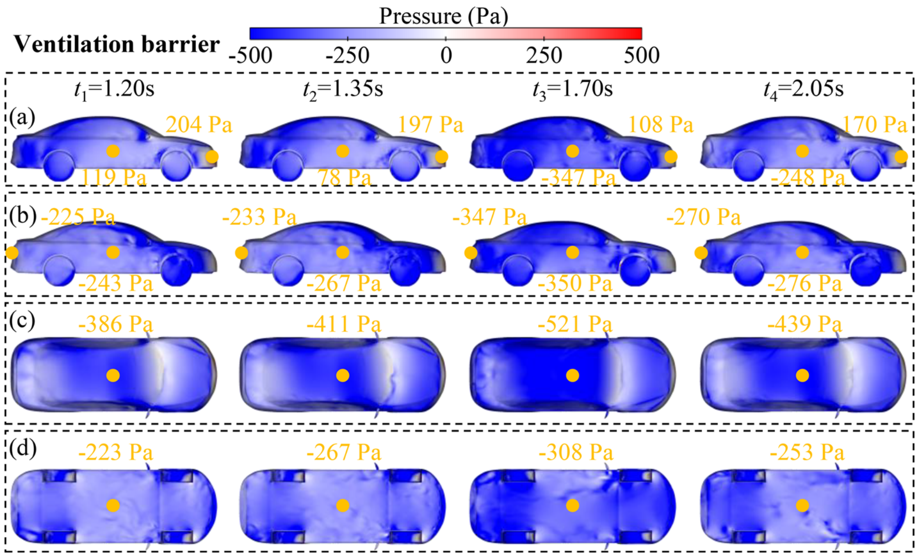

FIG. 20. Surface pressure cloud diagram of the vehicle with the ventilation wind barrier: (a) windward side; (b) leeward side; (c) top; and (d) bottom.

vehicle enters the hill section (t_2 moment), the body and the rear of the vehicle have not yet fully entered the hill, but due to the influence of the hill, the vortex on the right side moves above the vehicle. The airflow flows rapidly along the leeward side and the top, subjecting them to large negative pressure. As for the front of the vehicle, the further the vehicle enters the hill, the more the crosswind is affected by the turbulence caused by the wind barrier and hill. This results in a significant change in wind direction, with the crosswind at the cross section becoming $+Z$ direction, causing positive pressure on the windward side of the front of the vehicle. As the vehicle completely enters the hill section (t_3 moment), the turbulence effect of the hill and wind barrier on the crosswind intensifies further. Multiple positions in the cross-sectional flow field experience sudden changes in wind direction, leading to a significant increase in vortex structure and a noticeable alteration in surface pressure of the vehicle. When the vehicle drives out of the hill section (t_4 moment), it gradually leaves the hill range, and a large vortex can be observed on the right side of the vehicle. The crosswind acts obliquely on the leeward side of the vehicle and flows along the vehicle body, resulting in most of the vehicle's surface being subjected to negative pressure. However, the cross sections of the vehicle body and the rear wheel still remain within the range of the hill, leading to significant turbulence and the presence of many small vortex structures.

For the ventilation wind barrier condition, during the flat section (t_1 moment), when the crosswind blows to the windward side of the wind barrier, the wind barrier blocks the wind parallel to its direction (X and Y directions), allowing only the wind perpendicular to its direction (Z direction) to flow through. However, the wind speed decreases. As the low-speed wind impacts the windward side of the vehicle, it results in positive pressure. Flow separation takes place on the leeward side of the vehicle once the airflow passes over the vehicle, resulting in negative pressure on that side. The pressure distribution law is similar to that without wind barrier, but the pressure is smaller. When the vehicle enters the hill section (t_2 moment), the low height of the hill has little effect on the crosswind, resulting in a similar flow field structure to the t_1 moment, causing minimal changes in surface pressure on the vehicle. As the vehicle completely enters the hill section (t_3 moment), the turbulence caused by the hill and wind barrier leads to a significant increase in the size and number of vortex structures near the vehicle body. Particularly, several large vortex structures form near the leeward side, resulting in decreased surface pressure on the vehicle. When the vehicle drives out of the hill (t_4 moment), the hill has minimal impact on the crosswind, and the flow field structure around the vehicle closely resembles that observed when the vehicle initially encounters the hill section (t_1 moment), resulting in minimal changes in surface pressure on the vehicle.

In summary, when the vehicle passes by the hill with different windproof measures, the flow field structure around the vehicle is significantly affected. Without wind barrier, the crosswind directly affects the windward side of the vehicle, leading to flow separation on the leeward side. This amplifies the pressure differential between the two sides of the vehicle. Additionally, the sheltering effect of the hill alters the crosswind speed acting on the vehicle, leading to changes in pressure. Under ventilated wind barrier, the changes in the flow field structure are similar to those without wind barrier, but the wind barrier reduces the crosswind acting on the vehicle, resulting in more subdued pressure fluctuations on the vehicle's surface. Under solid wind barrier, the wind barriers cause the direction of the crosswind acting on the vehicle to reverse and intensify the turbulence, leading to disordered wind directions and alternating pressure changes on the vehicle's surface.

E. Transient vortex structure evolution

The presence of the hill and wind barriers alters the original flow field structure of crosswinds, making the changes more complex. To further reveal the impact of the hill and wind barriers on the flow field structure, Fig. 24 visually portrays the dynamic changes in vortex structures near the vehicle at four pivotal instances ($Q = 10\,000$). The vorticity diagram is colored with wind speed in the Z direction and is normalized with respect to the incoming wind speed ($U = 20$ m/s).

Analyzing Fig. 24 reveals that: in the condition of without wind barrier, a substantial number of separation vortex structures develop

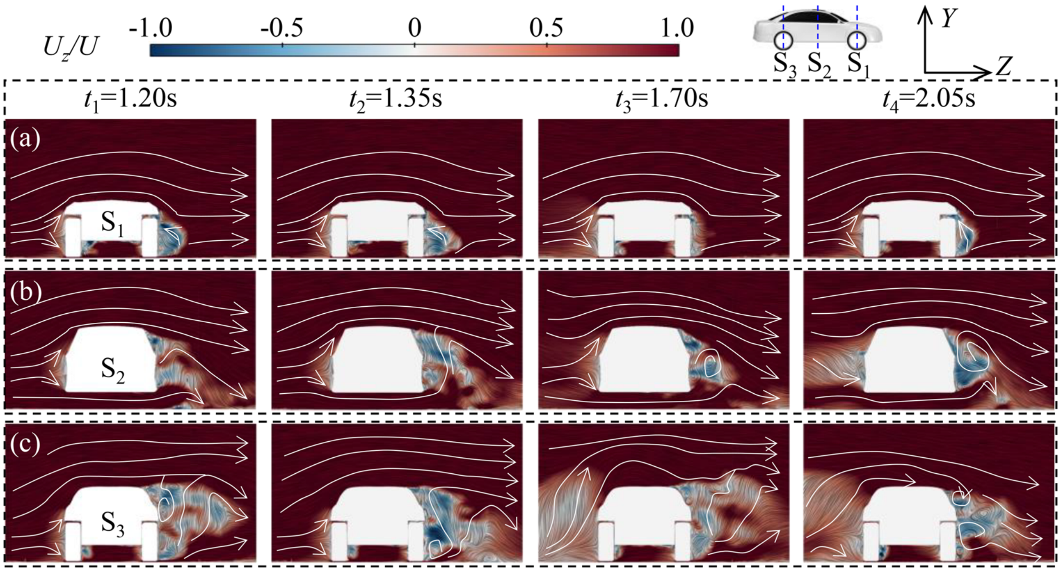

FIG. 21. Cross-sectional flow field structure of the vehicle without wind barrier: (a) front wheels; (b) mid-body; and (c) rear wheels.

on the leeward side of the vehicle during the flat section (t_1 moment), shedding at an angle of approximately 45° in the opposite direction of the vehicle's motion. Some of these vortex structures fall off and disappear as the vehicle continues to move. The vortex structures play a pivotal role in dissipating flow energy on the leeward side of the vehicle, embodying the typical characteristics of the flow field structure near the vehicle in crosswind conditions. When the vehicle enters the hill section (t_2 moment), the turbulence caused by the hill affects the crosswind, resulting in the capture of vortex structures in front of the vehicle. The shedding effect of vortex structures on the leeward side of the vehicle becomes more prominent, contributing to a heightened variability in the aerodynamic load. As the vehicle completely enters the hill section (t_3 moment), the increase in the height of the hill further intensifies the turbulence effect on the crosswind, leading to the formation of a large vortex structure at the top of the vehicle. The separation of vortex structures on the leeward side of the vehicle becomes more pronounced, leading to the most pronounced variations in the aerodynamic load. However, owing to the hill's shielding effect against crosswinds, the wind speed on the windward side decreases, resulting in diminished energy and aerodynamic load. When the vehicle drives out of the hill section (t_4 moment), the height of the hill gradually decreases, exposing the vehicle to the crosswind. The turbulence effect

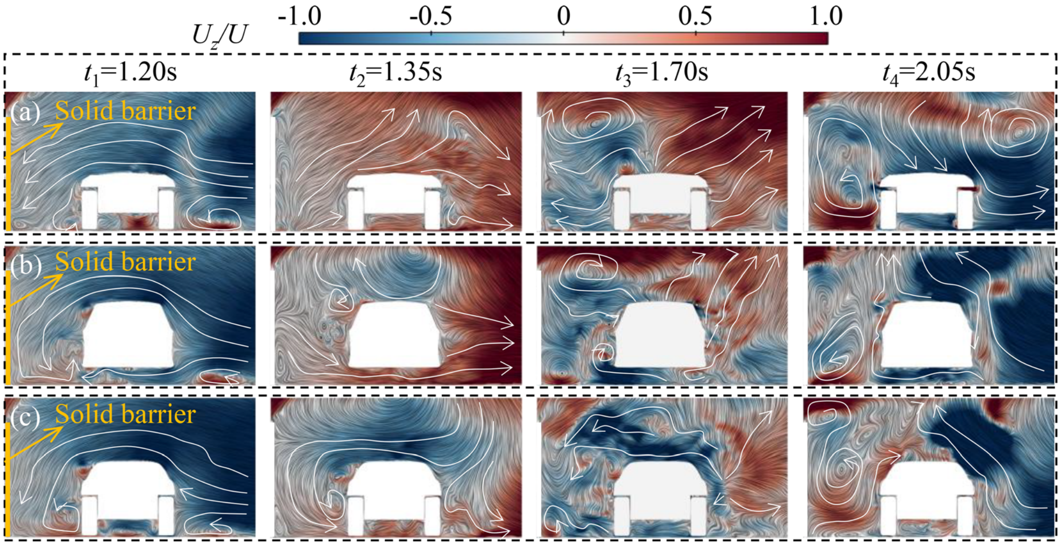

FIG. 22. Cross-sectional flow field structure of the vehicle with solid wind barrier: (a) front wheels; (b) mid-body; and (c) rear wheels.

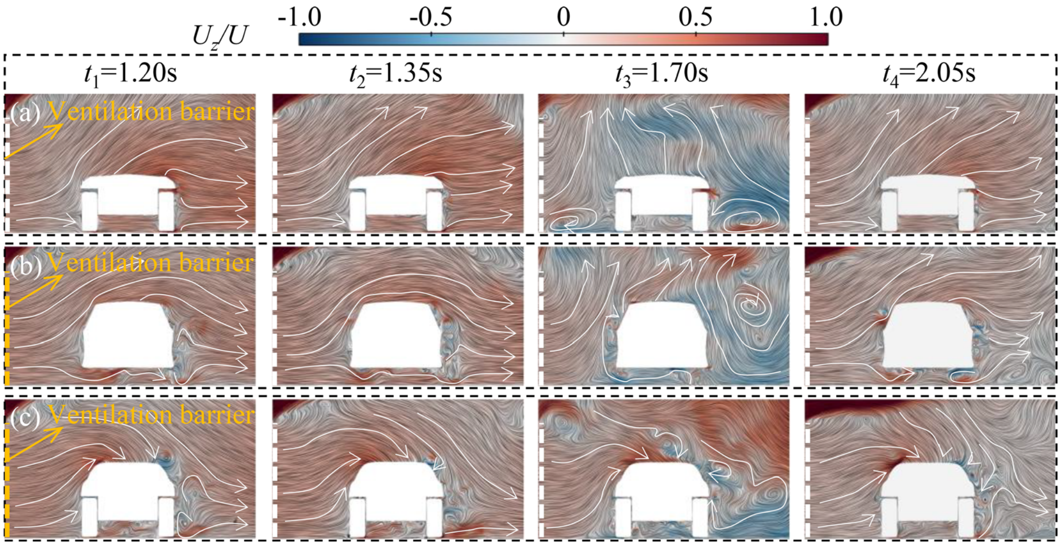

FIG. 23. Cross-sectional flow field structure of the vehicle with ventilation wind barrier: (a) front wheels; (b) mid-body; and (c) rear wheels.

of the hill diminishes, leading to a decrease in the number of vortex structures and a decrease in the variability of aerodynamic load fluctuations.

In the presence of a solid wind barrier, its primary function is to shield crosswinds during the flat section (t_1 moment). The quantity of vortex structures on the wind-facing side of the vehicle surpasses that on the leeward side, but their size is small, resulting in minimal fluctuation in aerodynamic load. It is worth noting that due to the vehicle's high driving speed, a significant number of detached vortex structures can still be observed directly behind the rear of the vehicle. When the vehicle enters the hill section (t_2 moment), the turbulent effect of the wind barrier on the crosswind becomes more pronounced, leading to an increased number of vortex structures near the front of the leeward side and the rear of the windward side of the vehicle. The fluctuation range of aerodynamic load increases, and the shedding angle of the rear vortex structure is approximately $-45°$ opposite to the running direction. As the vehicle completely enters the hill section (t_3 moment), under the combined turbulence of the hill and wind barrier, the size and number of vortex structures near the vehicle body significantly increase, resulting in drastic changes in aerodynamic load. The peak value of the power spectral density (PSD) is the largest, but the corresponding frequency is the smallest. When the vehicle drives out of the hill section (t_4 moment), the number and size of vortex structures near the body begin to decrease, leading to a decrease in the fluctuation range of aerodynamic load.

Under the ventilation wind barrier condition, the separation vortex structure can be observed on the leeward side of the vehicle during the process of driving by the hill, with the number initially decreasing and then increasing. The separation vortex structure at the rear of the vehicle is approximately parallel to the vehicle's driving direction. During the flat section (t_1 moment), the leeward side has the highest number of separation vortex structures, resulting in the largest energy dissipation, and the largest lateral force acting on the vehicle. Conversely, as the vehicle completely enters the hill section (t_3 moment), the number of leeward side vortex structures decreases, resulting in the smallest energy difference and a trough in lateral force. It is noteworthy that when the vehicle is driving under the ventilation wind barrier, the vortex structures are small and dense, resulting in the smallest fluctuation range in aerodynamic load and the smallest PSD peak, but the frequency is the highest.

In summary, when the vehicle drives by the hill with different windproof measures, the disparity in vortex structure distribution around the vehicle body is notably pronounced. Without wind barrier and with the ventilation wind barrier, more vortex structures emerge on the leeward side and in proximity to the rear of the vehicle as it traverses the hill. However, the dimensions and quantity of vortex structures are much smaller under the ventilation wind barrier condition compared to without wind barrier, resulting in smaller amplitude of aerodynamic load variation, the smallest PSD peak, but the highest frequency. Under the solid wind barrier condition, the position and size of vortex structures change with the vehicle's driving process. There are moments when vortex structures appear on the windward side, leeward side, top, and rear of the vehicle. The aerodynamic load exhibits its greatest extent of variation, and the PSD peak is the largest, but the frequency is the lowest.

V. CONCLUSIONS

Based on the improved delayed detached eddy simulation (IDDES) turbulence model, a refined three-dimensional computational fluid dynamics (CFD) numerical model of hill–embankment–wind barrier–vehicle–air system is established. The study delves into how hills impact the aerodynamic performance of high-speed vehicles in crosswind conditions. It also analyzes the variations in aerodynamic performance based on different windproof measures. In summary of the main points, we can conclude the following:

1. When a vehicle passes by a hill under the crosswind, its aerodynamic loads undergo complex and significantly increased variations, leading to a deterioration in aerodynamic performance.

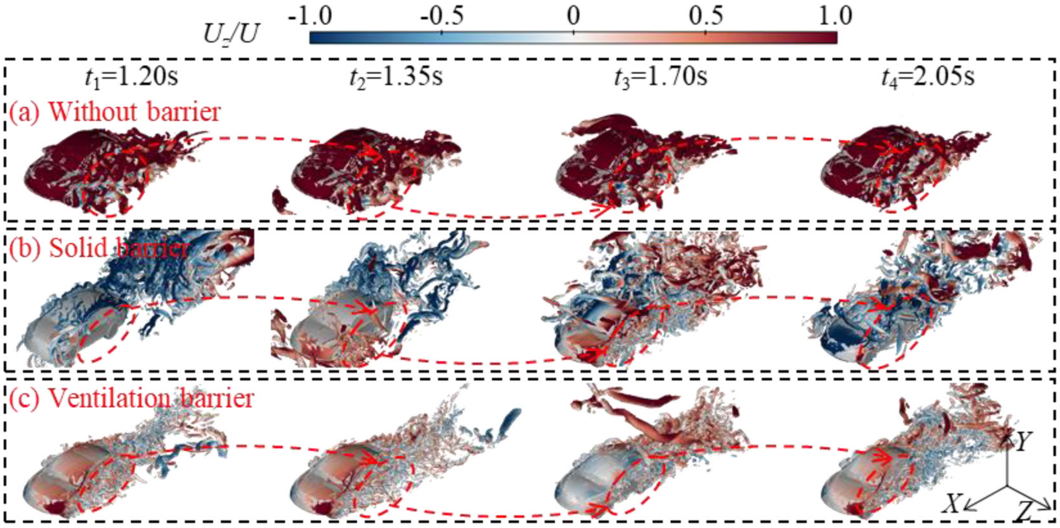

FIG. 24. Evolution of vortex structure: (a) without wind barrier; (b) solid wind barrier; and (c) ventilation wind barrier.

ΔC_x, ΔC_y, ΔC_z, ΔC_{mx}, ΔC_{my}, and ΔC_{mz} during the vehicle passing by the hill section without wind barrier are 2.79, 4.42, 5.18, 3.73, 4.45, and 2.73 times higher than those in the flat section, while σC_x, σC_y, σC_z, σC_{mx}, σC_{my}, and σC_{mz} are 2.25, 4.82, 5.88, 3.09, 5.04, and 2.98 times higher. The aerodynamic load on the vehicle increases linearly in response to increments in both vehicle speed and wind speed.

2. The fluctuation amplitude of the aerodynamic loads and the maximum value of power spectral density (PSD) are the greatest under the solid wind barrier, followed by without wind barrier condition, and the least under the ventilation wind barrier. Under the solid wind barrier, ΔC_x, ΔC_y, ΔC_z, ΔC_{mx}, ΔC_{my}, and ΔC_{mz} are 3.48 (3.63), 1.61 (2.16), 2.26 (4.34), 0.95 (2.93), 1.21 (2.00), and 3.88 (3.21) times that without wind barrier (with ventilation wind barrier). The PSD maxima are 1.49 (4.52), 1.31 (2.58), 2.12 (3.41), 1.59 (2.95), 1.79 (2.46), and 1.91 (2.58) times.
3. Under the condition of without wind barrier, the vehicle is subjected to high surface pressure, resulting in large peak values and fluctuations in the aerodynamic load. With the ventilation wind barrier, it shows similar surface pressure changes to without wind barrier but with smaller peak values and fluctuations. With the solid wind barrier, the average pressure difference between the opposing surfaces of the vehicle is larger, even exhibiting pressure inversion phenomena.
4. The presence of different windproof measures significantly impacts the flow field around a vehicle as it passes by a hill. Without wind barrier, crosswinds directly impact the windward side, causing flow separation on the leeward side. The hill's shelter also changes the crosswind speed, affecting pressure on the vehicle. A ventilated wind barrier reduces crosswind effects, leading to less pressure fluctuation. A solid wind barrier reverses the crosswind direction, increases turbulence, and results in more erratic wind patterns and pressure changes on the vehicle's surface.
5. The distribution of vortex structures near the vehicle's body is highly significant when passing by the hill under different windproof measures. Without wind barrier and with ventilation wind barrier, more vortex structures appear on the leeward side and behind the vehicle. The size and number of vortex structures are much smaller with ventilation wind barrier compared to without wind barrier. With solid wind barrier, the position and size of vortex structures continuously change as the vehicle progresses, leading to the most significant alterations in aerodynamic loads.

It is important to note that this study only considers the variation of aerodynamic load and flow field structure when the vehicle passes by the hill under the influence of pure wind. However, many windy areas also contain solid particles, such as sand. In the subsequent study, we can evaluate the influence of sand on vehicle safety and evaluate the driving safety of vehicles under different sand particle sizes and concentrations.

ACKNOWLEDGMENTS

This work was funded by the National Natural Science Foundation of China [Grant Number 52308419]; the Science and Technology Research and Development Program Project of China railway group limited [Major Special Project, 2021-Special-04-2]; the Science and Technology Research and Development Program Project of China railway group limited [Major Project, 2021-Major-01]; the Science and Technology Research and Development Program Project of China railway group limited [Major Project, 2022-Key-23]; and the Innovation and Technology Commission of Hong Kong, China [Grant Number K-BBY1].

AUTHOR DECLARATIONS

Conflict of Interest

The authors have no conflicts to disclose.

Author Contributions

Hong He: Software (lead), Writing-original draft (lead). **Guo-Zhi Li**: Software (equal), Writing-original draft (equal), Writing-review & editing (equal). **Wei-Chao Yang**: Conceptualization (lead), Funding acquisition (lead), Project administration (lead), Writing-review & editing (equal). **Yi-Kang Liu**: Writing-review & editing (equal). **E Deng**: Methodology (lead), Data curation (lead), Writing-review & editing (lead), Supervision (lead), Funding acquisition (equal).

DATA AVAILABILITY

The data that support the findings of this study are available from the corresponding author upon reasonable request.

REFERENCES

[1] Q. W. Zhang, C. Q. Su, and Y. P. Wang, "Numerical investigation on aerodynamic performance and stability of a sedan under wind–bridge–tunnel road condition," Alexandria Eng. J. **59**, 3963–3980 (2020).

[2] A. Brandt, B. Jacobson, and S. Sebben, "High speed driving stability of road vehicles under crosswinds: An aerodynamic and vehicle dynamic parametric sensitivity analysis," Veh. Syst. Dyn. **60**, 2334–2357 (2022).

[3] L. D. Zhu, L. Li, Y. L. Xu, and Q. Zhu, "Wind tunnel investigations of aerodynamic coefficients of road vehicles on bridge deck," J. Fluids Struct. **30**, 35–50 (2012).

[4] W. C. Yang, L. Zhao, E. Deng, Y. Q. Ni, W. Zhao, Y. K. Liu, and D. H. Ouyang, "Spatial-temporal characteristics of the transient flow field around high-speed trains transiting the subgrade-cutting transition section under crosswinds," Alexandria Eng. J. **86**, 34–48 (2024).

[5] D. Zhou, D. Z. Yu, L. L. Wu, and S. Meng, "Numerical investigation of the evolution of aerodynamic behaviour when a high-speed train accelerates under crosswind conditions," Alexandria Eng. J. **72**, 51–66 (2023).

[6] Y. F. Zou, Z. P. Liu, K. Shi, X. H. He, S. Zhou, and W. R. Ma, "Analysis of effects of aerodynamic interference on dynamic response of suspended monorail wind–vehicle–bridge system using joint simulation approach," Structures **45**, 179–198 (2022).

[7] S. Kim, H. Y. Cheon, S. Jung, and H. K. Kim, "Wind-induced accidents on the transition section of a cable-stayed bridge: Cause and remedy," J. Bridge Eng. **29**, 05023013 (2024).

[8] J. L. Chen and F. Chen, "Efficient vehicle lateral safety analysis based on Multi-Kriging metamodels: Autonomous trucks under different lateral control modes during being overtaken," Accid. Anal. Prev. **208**, 107787–107787 (2024).

[9] S. R. Chen and C. S. Cai, "Accident assessment of vehicles on long-span bridges in windy environments," J. Wind Eng. Ind. Aerodyn. **92**, 991–1024 (2004).

[10] Q. W. Zhang, C. Q. Su, M. Tsubokura, Z. Hu, and Y. P. Wang, "Coupling analysis of transient aerodynamic and dynamic response of articulated heavy vehicles under crosswinds," Phys. Fluids **34**, 212013 (2022).

[11] M. Batista and M. Perkovič, "A simple static analysis of moving road vehicle under crosswind," J. Wind Eng. Ind. Aerodyn. **128**, 105–113 (2014).

[12] M. Tsubokura, T. Nakashima, M. Kitayama, Y. Ikawa, D. Doh, and T. Kobayashi, "Large eddy simulation on the unsteady aerodynamic response of a road vehicle in transient crosswinds," Int. J. Heat Fluid Flow **31**, 1075–1086 (2010).

[13] L. N. Liu, Y. M. Sun, X. F. Chi, G. S. Du, and M. Wang, "Transient aerodynamic characteristics of vans overtaking in crosswinds," J. Wind Eng. Ind. Aerodyn. **170**, 46–55 (2017).

[14] E. Ljungskog, S. Sebben, and A. Broniewicz, "Inclusion of the physical wind tunnel in vehicle CFD simulations for improved prediction quality," J. Wind Eng. Ind. Aerodyn. **197**, 104055 (2020).

[15] D. Sekulic, A. Vdovin, B. Jacobson, S. Sebben, and S. Johannesen, "Analysis of vehicle path tracking ability and lateral stability on a floating bridge under a crosswind," J. Wind Eng. Ind. Aerodyn. **227**, 105070 (2022).

[16] J. M. Zhang, C. M. Ma, R. Xian, J. K. Li, and Q. F. Li, "Wind tunnel investigations of crosswind loads for static road vehicles on wide bridge decks," J. Wind Eng. Ind. Aerodyn. **233**, 105315 (2023).

[17] B. Wang, Y. L. Xu, L. D. Zhu, and Y. L. Li, "Crosswind effect studies on road vehicle passing by bridge tower using computational fluid dynamics," Eng. Appl. Comput. Fluid Mech. **8**, 330–344 (2014).

[18] Y. P. Wang, Z. Y. Zhang, Q. W. Zhang, Z. Hu, and C. Q. Su, "Dynamic coupling analysis of the aerodynamic performance of a sedan passing by the bridge pylon in a crosswind," Appl. Math. Modell. **89**, 1279–1293 (2021).

[19] T. M. Huang, M. C. Feng, J. Huang, J. M. Ma, D. X. Yi, X. Ren, L. Zhang, and W. Zeng, "Aerodynamic stability of high-speed vehicle passing bridge tower in different lanes under crosswind conditions," J. Wind Eng. Ind. Aerodyn. **242**, 105560 (2023).

[20] T. M. Huang, M. C. Feng, J. Huang, J. M. Ma, D. X. Yi, X. Ren, L. Zhang, and C. J. Ou, "Aerodynamic stability of vehicle passing through a bridge tower at high speed under crosswind conditions with different road adhesion coefficients," Alexandria Eng. J. **77**, 461–478 (2023).

[21] H. L. Yu, B. Wang, Y. L. Li, and M. J. Zhang, "Driving risk of road vehicle shielded by bridge tower under strong crosswind," Nat. Hazards **96**, 497–519 (2019).

[22] Z. W. Chen, T. H. Liu, W. H. Li, Z. J. Guo, and Y. T. Xia, "Aerodynamic performance and dynamic behaviors of a train passing through an elongated hillock region beside a windbreak under crosswinds and corresponding flow mitigation measures," J. Wind Eng. Ind. Aerodyn. **208**, 104434 (2021).

[23] C. Q. Su, Z. Hu, Q. W. Zhang, X. H. Yuan, C. C. Zhang, and Y. P. Wang, "Coupling analysis of transient aerodynamic and dynamic response of cars in overtaking under crosswinds," Eng. Appl. Comp. Fluid Mech. **14**, 1215–1227 (2020).

[24] A. Hammad, T. Xing, A. Abdel-Rahim, V. Durgesh, and J. C. Crepeau, "Effect of crosswinds on the aerodynamics of two passenger cars crossing each other," Int. J. Automot. Technol. **20**, 997–1008 (2019).

[25] Y. F. Zou, F. R. Xue, K. Shi, X. H. He, Y. Han, Q. K. Liu, and L. F. Li, "Analysis of the effects of wind barrier on driving safety and comfort of vehicles on long-span bridges under crosswinds," Structures **42**, 367–385 (2022).

[26] A. Camara, L. Fernandez-Elvira, C. Stroumpouli, and C. Jagadeesh, "Skew wind actions on vehicles crossing bridges with solid parapets," J. Wind Eng. Ind. Aerodyn. **240**, 105485 (2023).

[27] M. Xu, L. Patruno, Y. Lo, and S. de Miranda, "Simulation strategies for wind shields and porous barriers for bridge deck optimization," Structures **40**, 824–839 (2022).

[28] N. Chen, Y. L. Li, B. Wang, Y. Su, and H. Y. Xiang, "Effects of wind barrier on the safety of vehicles driven on bridges," J. Wind Eng. Ind. Aerodyn. **143**, 113–127 (2015).

[29] D. L. Wang, M. J. Sun, X. Shen, and A. R. Chen, "Aerodynamic characteristics and structural behavior of sound barrier under vehicle-induced flow for five typical vehicles," J. Fluids Struct. **117**, 103816 (2023).

[30] F. R. Xue, Y. Han, Y. F. Zou, X. H. He, and S. R. Chen, "Effects of wind-barrier parameters on dynamic responses of wind-road vehicle–bridge system," J. Wind Eng. Ind. Aerodyn. **206**, 104367 (2020).

[31] H. Y. Xiang, Y. L. Li, S. R. Chen, and G. Y. Hou, "Wind loads of moving vehicle on bridge with solid wind barrier," Eng. Struct. **156**, 188–196 (2018).

[32] Y. X. Yang, J. J. Zhang, F. C. Cao, Y. J. Ge, and L. Zhao, "Evaluation and improvement of wind environment and vehicle safety on long-span bridge deck under strong crosswind," J. Wind Eng. Ind. Aerodyn. **228**, 105089 (2022).

[33] C. R. Chu, C. Y. Chang, C. J. Huang, T. R. Wu, C. Y. Wang, and M. Y. Liu, "Windbreak protection for road vehicles against crosswind," J. Wind Eng. Ind. Aerodyn. **116**, 61–69 (2013).

[34] H. He, W. C. Yang, Y. K. Liu, and E. Deng, "Three-dimensional trajectories of irregular-shaped tunnel lining fragments in the flow environment caused by high-speed trains," Phys. Fluids **36**, 085193 (2024).

[35] O. El Moctar, U. Lantermann, V. Shigunov, and T. E. Schellin, "Experimental and numerical investigations of effects of ship superstructures on wind-induced loads for benchmarking," Phys. Fluids **35**, 045124 (2023).

[36] W. C. Yang, J. Wang, and Y. Dong, "Effectiveness of three turbulence modeling approaches in a crosswind–sedan–dune computational fluid dynamics framework," Appl. Sci.-Basel **14**, 7522 (2024).

[37] J. Munoz-Paniagua, J. García, and B. Lehugeur, "Evaluation of RANS, SAS and IDDES models for the simulation of the flow around a high-speed train subjected to crosswind," J. Wind Eng. Ind. Aerodyn. **171**, 50–66 (2017).

[38] T. Maruyama, "Large eddy simulation of turbulent flow around a windbreak," J. Wind Eng. Ind. Aerodyn. **96**, 1998–2006 (2008).

[39] L. Zhao, W. C. Yang, Y. K. Liu, and E. Deng, "Effects of windbreak types on aerodynamics of high-speed trains traversing from flat ground to semi-cutting and semi-embankment under crosswinds," Phys. Fluids **36**, 075115 (2024).

[40] Y. Wang, K. Zhong, J. Hu, and Y. Kang, "An anisotropic prediction model of the resistance coefficient in porous media model for simulating wind flow through building arrays," Build. Environ. **228**, 109807 (2023).

[41] E. Deng, W. Yang, X. He, Z. Zhu, H. Wang, Y. Wang, A. Wang, and L. Zhou, "Aerodynamic response of high-speed trains under crosswind in a bridge-tunnel section with or without a wind barrier," J. Wind Eng. Ind. Aerodyn. **210**, 104502 (2021).

[42] W. C. Yang, D. H. Ouyang, E. Deng, Y. W. Wang, Z. W. Chen, X. H. He, and Y. M. Huang, "Deterioration of aerodynamic performance of a train driving through noise barriers under crosswinds," J. Wind Eng. Ind. Aerodyn. **231**, 105241 (2022).

[43] E. Deng, X. Y. Liu, H. Yue, W. C. Yang, D. H. Ouyang, and Y. Q. Ni, "How do dunes along a desert urban motorway affect the driving safety of sedans? Evidences from long- and short-term monitoring and IDDES," J. Wind Eng. Ind. Aerodyn. **243**, 105595 (2023).

[44] H. Y. Xiang, Y. L. Li, S. R. Chen, and C. J. Li, "A wind tunnel test method on aerodynamic characteristics of moving vehicles under crosswinds," J. Wind Eng. Ind. Aerodyn. **163**, 15–23 (2017).

[45] J. Q. Niu, Y. C. Zhang, R. Li, Z. W. Chen, H. D. Yao, and Y. M. Wang, "Aerodynamic simulation of effects of one- and two-side windbreak walls on a moving train running on a double track railway line subjected to strong crosswind," J. Wind Eng. Ind. Aerodyn. **221**, 104912 (2022).